

# Performance of the $r^2$ SCAN Functional in Transition Metal Oxides

S. Swathilakshmi, Reshma Devi, and Gopalakrishnan Sai Gautam\*



Cite This: <https://doi.org/10.1021/acs.jctc.3c00030>



Read Online

ACCESS |



Metrics & More

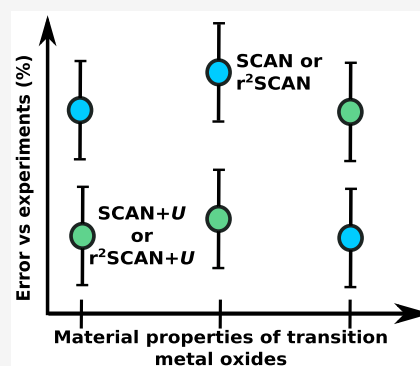


Article Recommendations



Supporting Information

**ABSTRACT:** We assess the accuracy and computational efficiency of the recently developed meta-generalized gradient approximation (metaGGA) functional, restored regularized strongly constrained and appropriately normed ( $r^2$ SCAN), in transition metal oxide (TMO) systems and compare its performance against SCAN. Specifically, we benchmark the  $r^2$ SCAN-calculated oxidation enthalpies, lattice parameters, on-site magnetic moments, and band gaps of binary 3d TMOs against the SCAN-calculated and experimental values. Additionally, we evaluate the optimal Hubbard  $U$  correction required for each transition metal (TM) to improve the accuracy of the  $r^2$ SCAN functional, based on experimental oxidation enthalpies, and verify the transferability of the  $U$  values by comparing against experimental properties on other TM-containing oxides. Notably, including the  $U$ -correction with  $r^2$ SCAN increases the lattice parameters, on-site magnetic moments, and band gaps of TMOs, apart from an improved description of the ground state electronic state in narrow band gap TMOs. The  $r^2$ SCAN and  $r^2$ SCAN+ $U$  calculated oxidation enthalpies follow the qualitative trends of SCAN and SCAN+ $U$ , with  $r^2$ SCAN and  $r^2$ SCAN+ $U$  predicting marginally larger lattice parameters, smaller magnetic moments, and lower band gaps compared to SCAN and SCAN+ $U$ , respectively. We observe the overall computational time (i.e., for all ionic+electronic steps) required for  $r^2$ SCAN(+ $U$ ) to be lower than SCAN(+ $U$ ). Thus, the  $r^2$ SCAN(+ $U$ ) framework can offer a reasonably accurate description of the ground state properties of TMOs with better computational efficiency than SCAN(+ $U$ ).



## 1. INTRODUCTION

Density functional theory (DFT<sup>1</sup>) calculations are the bedrock of modern computational materials science in terms of predicting thermodynamic and kinetic properties, with such property predictions being put to use in subsequent materials discovery<sup>2–7</sup> and understanding underlying physical phenomena.<sup>8–12</sup> In recent years, machine learning has been used to augment DFT in property predictions, thereby reducing computational cost and accelerating materials discovery.<sup>13–17</sup> Note that a key approximation within DFT is the exchange–correlation (XC) functional, the exact form of which is unknown. However, several approximations for the XC functional have been proposed over the years, which can be categorized into different classes depending on the degree of sophistication and accuracy, and visually represented as rungs on Jacob’s ladder.<sup>1,2,18,19</sup> As with most computational tools, the higher the accuracy (higher up Jacob’s ladder) the higher the computational cost.

Most DFT calculations for “large” solid systems (10 s to 100 s of atoms) are performed using the Perdew–Burke–Ernzerhof (PBE) parametrization of the generalized gradient approximation (GGA) XC functional,<sup>20</sup> as it offers fair accuracy at reasonable computational cost for a wide variety of materials.<sup>21–23</sup> Specifically, GGAs include the local electron density as well as the gradient of the electron density in describing the XC. As a semilocal functional of electron density, PBE captures short-range interactions but fails to

capture medium- and long-range dispersions and also exhibits large electronic self-interaction errors (SIEs), especially in highly correlated systems.<sup>24,25</sup> Also, PBE typically underestimates the formation energies<sup>26,27</sup> and semiconductor band gaps of crystalline solids,<sup>26,28</sup> while overestimating their lattice volumes.<sup>26,29</sup>

As we move higher in Jacob’s ladder,<sup>19</sup> we obtain metaGGA functionals, which may account for medium range dispersions and exhibit lower SIEs. Some metaGGAs consider orbital kinetic energy density in addition to the local electron density and its gradient, such as the recently developed strongly constrained and appropriately normed (SCAN<sup>30</sup>) functional, which offers better numerical accuracy than PBE and satisfies all 17 known constraints for an XC functional (namely, 6 for exchange, 6 for correlation, and 5 for both). The iso-orbital indicator ( $\alpha$ ), which includes the kinetic energy density in SCAN, distinguishes various bonding environments in a given material and consequently improves the accuracy of SCAN over GGA. However, SCAN suffers from numerical instability during self-consistent-field (SCF) calculations<sup>31</sup> wherein

Received: January 8, 2023

denser  $k$ -grids (than PBE) are required for accurate and consistent predictions.<sup>31–33</sup> Thus, it is computationally expensive (per SCF step) compared to PBE.<sup>21</sup>

To overcome the numerical instability and reduce the computational cost of SCAN, Bartok and Yates<sup>34</sup> developed regularized SCAN (rSCAN), which satisfies 13 out of the 17 known constraints. The authors replaced the nonanalytical switching  $\alpha$  interpolation function in SCAN with a simple polynomial function, which improves computational speed.<sup>35</sup> However, subsequent investigations showed a significant drop in numerical accuracy with rSCAN (compared to SCAN), which is attributed to the failure of the polynomial  $\alpha$  function to fully recover the uniform gas limit.<sup>31,32</sup> Subsequently, Furness et al.<sup>32</sup> introduced the restored regularized SCAN (or r<sup>2</sup>SCAN), wherein the constraints broken by rSCAN were restored except the fourth order gradient expansion constraint for exchange (or GE4X). Furness et al. claimed that the new r<sup>2</sup>SCAN functional combines the numerical accuracy of SCAN and computational speed of rSCAN as the smooth polynomial  $\alpha$  function of rSCAN is modified to satisfy the uniform gas limit in r<sup>2</sup>SCAN.<sup>32</sup>

Recently, Kingsbury et al.<sup>36</sup> demonstrated that the r<sup>2</sup>SCAN functional indeed delivers robust numerical accuracy (i.e., similar to SCAN) and better computational performance (faster and numerically stable) by comparing r<sup>2</sup>SCAN and SCAN for solids using a high-throughput computational workflow. Specifically, the authors<sup>36</sup> reported that while r<sup>2</sup>SCAN predicts a smaller band gap (for most of the strongly bound materials) and larger lattice volumes than SCAN, the mean atomization error with r<sup>2</sup>SCAN is  $\sim 15$ – $20\%$  lower for most solids. Similarly, Kothakonda et al.<sup>37</sup> demonstrated that r<sup>2</sup>SCAN offered improved accuracy over SCAN in predicting formation enthalpies with and without dispersion corrections for a range of intermetallics, oxides, and transition metal compounds, while r<sup>2</sup>SCAN overestimated lattice volumes and underestimated band gaps with respect to experiments in the same set of compounds the authors considered. However, the performance of r<sup>2</sup>SCAN in correlated electron systems, i.e., transition metal oxides (TMOs) containing open-shell  $d$  electrons, remains to be seen and forms the main focus of this work.

Despite the accuracy of SCAN, it still has shortcomings in TMOs, which can be mitigated by adding an on-site Hubbard  $U$  correction term for the transition metal (TM) under consideration.<sup>38,39</sup> This approach is similar to the one followed to mitigate the SIEs of PBE in TMOs.<sup>40,41</sup> However, the magnitude of the  $U$  correction required is not known *a priori*, and there are both theory-based approaches such as density functional perturbation theory,<sup>42</sup> linear response theory,<sup>43–45</sup> embedded Hartree–Fock method,<sup>46,47</sup> and machine learning based Bayesian optimization<sup>48</sup> and experimental-data-based approaches to identify the appropriate  $U$  values. For example, Artrith et al.<sup>49</sup> demonstrated the use of robust statistical methodologies such as regularized least-squares optimization, cross-validation, principal component analysis, and  $k$ -means clustering to determine and validate optimized Hubbard  $U$  corrections for the SCAN functional in the prediction of formation energies of the binary and ternary TM oxides. Gautam et al.<sup>38,39</sup> used the experimental oxidation enthalpies among binary TMOs to identify optimal  $U$  values across various oxidation states of  $3d$  TMs. A similar experimental-data-based Hubbard  $U$  correction scheme can be developed in conjunction with r<sup>2</sup>SCAN as well, resulting in an r<sup>2</sup>SCAN+ $U$

framework, in case r<sup>2</sup>SCAN exhibits similar SIEs as SCAN in TMOs. We explore the usefulness of such an r<sup>2</sup>SCAN+ $U$  framework also in this work.

Here, we verify the numerical accuracy and computational efficiency of the r<sup>2</sup>SCAN and r<sup>2</sup>SCAN+ $U$  frameworks in comparison to SCAN and SCAN+ $U$ , respectively, in describing material properties such as lattice parameters, on-site magnetic moments, and band gaps of binary  $3d$  TMOs, including Ti, V, Cr, Mn, Fe, Co, Ni, and Cu. As necessary, we evaluate the optimal Hubbard  $U$  correction with r<sup>2</sup>SCAN for each TM by using the experimental-data-based approach employed in previous works.<sup>38,39</sup> We find that r<sup>2</sup>SCAN predicts marginally larger lattice constants and smaller on-site magnetic moments than SCAN for most of the TMOs considered. On addition of the  $U$ -correction to both SCAN and r<sup>2</sup>SCAN, we observe an increase in the calculated lattice constants, on-site magnetic moments, and band gaps. In the case of narrow band gap TMOs, SCAN+ $U$  and r<sup>2</sup>SCAN+ $U$  generally estimate a nonzero band gap, with r<sup>2</sup>SCAN+ $U$ 's band gap in better agreement with experiments. Also, we perform transferability checks for the optimal  $U$  values derived in this work for each TM, by benchmarking various properties in oxides that were not used in obtaining the  $U$  values. Finally, we compare the computational performance of r<sup>2</sup>SCAN/r<sup>2</sup>SCAN+ $U$  relative to SCAN/SCAN+ $U$  to explore the accuracy-cost trade-off. We report that r<sup>2</sup>SCAN/r<sup>2</sup>SCAN+ $U$  is computationally less expensive than SCAN and SCAN+ $U$ , when all required ionic and electronic steps are taken into account for convergence during structure relaxations. We hope that our work will provide a foundational basis for further studies on understanding material behavior and computationally discovering new materials in the near future.

## 2. METHODS

**2.1. Computational Methods.** We used the Vienna ab initio simulation package (VASP 6.2.1)<sup>50–52</sup> for all the spin-polarized DFT calculations, where the frozen-core PBE-based projector augmented wave (PAW)<sup>53</sup> potentials employed were identical to previous work.<sup>38,39</sup> The plane waves for each system were expanded up to a kinetic energy of 520 eV, with each structure converged until the total energy differences and atomic forces became  $<0.01$  meV and  $<0.01$  eV/Å, respectively. We adopted a  $\Gamma$ -centered Monkhorst–Pack<sup>54</sup> grid with a density of 48  $k$ -points per Å for all systems. Specifically, we determine the number of subdivisions in reciprocal space along a given lattice vector as the  $k$ -point density divided by the magnitude of the corresponding lattice vector, with any resultant fractional values rounded-up to the nearest integer. For example, a lattice vector of 4 Å will result in  $48/4 = 12$  subdivisions in the reciprocal space along its direction. The conjugate gradient algorithm was used to relax the structures (i.e., cell shapes, volumes, and ionic positions), without preserving any underlying symmetry. An “accurate” level of precision was maintained while projecting the wave functions in the reciprocal space. The Fermi surface of each system was integrated with a Gaussian smearing of partial occupancies, with a width of 0.05 eV. In terms of DFT+ $U$  calculations, we used the Dudarev framework<sup>55</sup> for adding an effective  $U$  correction on the  $d$  orbitals of TM atoms. All  $U$  values used in SCAN+ $U$  calculations were taken from previous work (see Table S1 of the Supporting Information).<sup>38,39</sup> Since we used different computing systems to perform our structure relaxations for different systems, we normalized the computa-

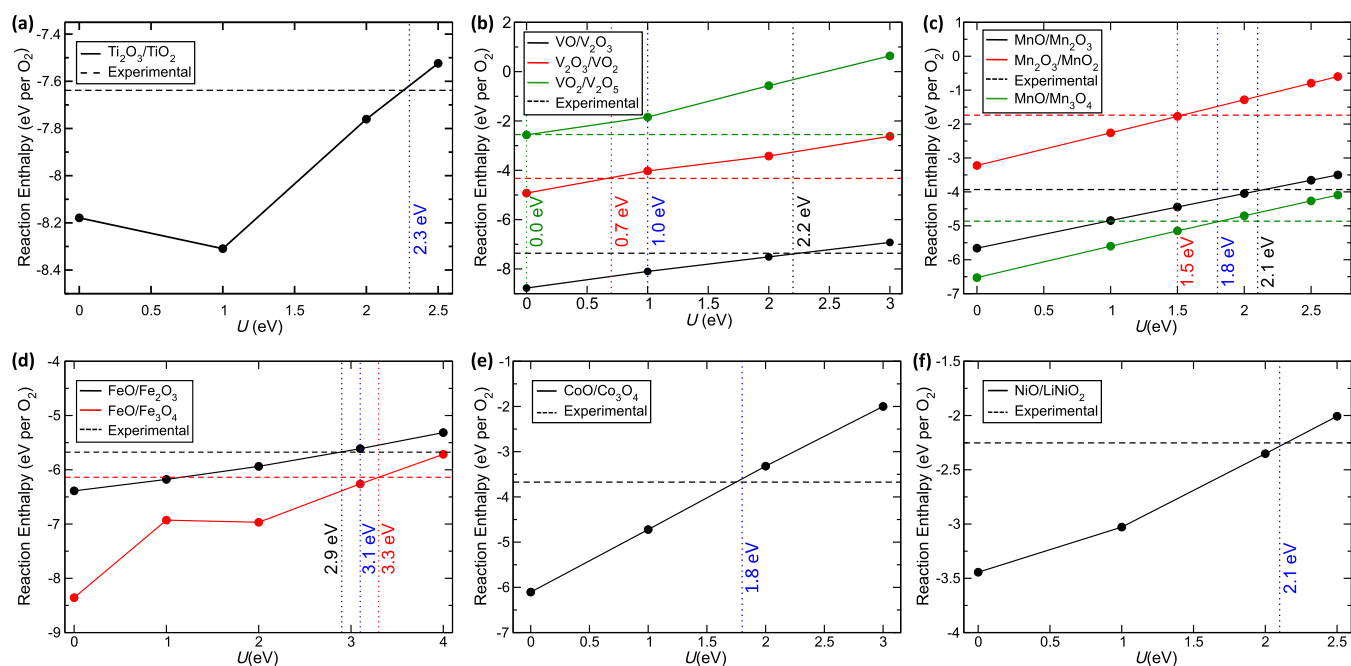


**Figure 1.** Calculated oxidation enthalpy versus the magnitude of  $U$  correction within the  $r^2$ SCAN+ $U$  framework for (a) Ti, (b) V, (c) Mn, (d) Fe, (e) Co, and (f) Ni oxides. Solid, dashed, and dotted lines of a given color indicate calculated, experimental, and required  $U$  values for a given oxidation reaction. Optimal  $U$  for each TM is indicated by the dotted blue line in each panel.

tional time with the number of cores used in each calculation to compare the computational efficiency of the different XC functionals considered.

For calculating band gaps, GGA functionals typically use the Kohn–Sham potential as a multiplicative term, which typically underestimates the band gap of solids even at the SCAN level.<sup>56,57</sup> Here, we use the generalized Kohn–Sham technique to determine the band gaps by calculating the density of states (DOS) for all systems considered. For each DOS calculation, we used the optimized structure and the initial charge density from a previous structure relaxation. Subsequently, we introduced a set of zero-weighted  $k$ -points, corresponding to a density of 96  $k$ -points per Å, where the  $k$ -points that were used for the structure relaxation retained their original weights (as determined by VASP). Finally, we performed a single-SCF calculation where the DOS was sampled between energies of  $-20$  to  $20$  eV in steps of 0.005 eV.

**2.2. Structures and Magnetic Configurations.** We considered the binary oxides of each TM, i.e., Ti, V, Cr, Mn, Fe, Co, Ni, and Cu with different oxidation states, similar to previous studies.<sup>38,39</sup> The main criteria in selection of these metal oxides are the availability of reliable thermodynamic data (i.e., formation energies<sup>58–60</sup>) and the experimentally determined ground-state structures that are compiled in the inorganic crystal structure database (ICSD).<sup>61</sup> Note that the structures from the ICSD were the initial structures in all our DFT structure relaxations, including the systems used as transferability checks. In the case of Ni oxides, we chose NiO and LiNiO<sub>2</sub> (similar to previous work<sup>39</sup>), as reliable thermodynamic data is not available for higher-oxidation-state binary Ni oxides (e.g., Ni<sub>2</sub>O<sub>3</sub> and NiO<sub>2</sub>). The TM in all oxides, except select Co and Ni compounds, was initialized in its high-spin configuration (e.g., high-spin configuration of Fe<sup>3+</sup> consists of five unpaired  $d$  electrons). A detailed description of all structures utilized in this work is provided in the SI, under

the “Crystal Structures” section, with the magnetic configurations depicted in Figure S1.

The magnetic configuration of each TMO considered (see Figure S1) was initialized to its appropriate (in several cases, experimentally known) ground state configuration during the structural relaxation. For example, we considered the ferromagnetic (FM) ground state configuration for CrO<sub>2</sub> and VO<sub>2</sub>, given that CrO<sub>2</sub> is metallic<sup>62</sup> and VO<sub>2</sub> undergoes a metal-to-insulator transition (MIT) below 341 K.<sup>63</sup> The rocksalt (RS) TMOs, namely, VO, MnO, FeO, CoO, and NiO, were initialized with their experimentally known type-II antiferromagnetic (AFM) configuration.<sup>64–69</sup> Each Ni’s spin in NiO was initialized with two unpaired  $d$  electrons (i.e., its high-spin configuration). In CuO, we arranged the magnetic moments of Cu<sup>2+</sup> antiferromagnetically along the Cu–O–Cu chains in the  $[10\bar{1}]$  direction.<sup>70,71</sup>

We initialized  $\alpha$ -Mn<sub>2</sub>O<sub>3</sub> (bixbyite structure) in an FM configuration as this configuration was found to be the most stable in previous work.<sup>38</sup> AFM configurations were utilized for rutile-MnO<sub>2</sub>,<sup>72</sup> and the other TM<sub>2</sub>O<sub>3</sub> oxides, namely, V<sub>2</sub>O<sub>3</sub>, Fe<sub>2</sub>O<sub>3</sub>, Ti<sub>2</sub>O<sub>3</sub>, and Cr<sub>2</sub>O<sub>3</sub>. Note that V<sub>2</sub>O<sub>3</sub> becomes AFM below its MIT temperature,<sup>73–75</sup> while Fe<sub>2</sub>O<sub>3</sub> displays an AFM configuration with the magnetic moment of Fe alternating every two consecutive layers along the  $c$ -axis.<sup>76</sup> Cr<sub>2</sub>O<sub>3</sub> and Ti<sub>2</sub>O<sub>3</sub> exhibit  $\uparrow\downarrow\uparrow\downarrow$  and  $\uparrow\downarrow\downarrow\uparrow$  magnetic configurations, respectively, on the TM centers along the  $a$ -axis.<sup>77,78</sup>

In the case of spinels, we used different ferrimagnetic (FIM) configurations, as per experimental observations. For example, spinel-Fe<sub>3</sub>O<sub>4</sub> contains both Fe<sup>3+</sup> and Fe<sup>2+</sup>, with up-spin Fe<sup>3+</sup> occupying tetrahedral sites and down-spin Fe<sup>3+</sup> occupying half the octahedral sites. The remaining octahedral sites in Fe<sub>3</sub>O<sub>4</sub> are occupied by up-spin Fe<sup>2+</sup>.<sup>79,80</sup> In Co<sub>3</sub>O<sub>4</sub>, no-spin Co<sup>3+</sup> occupies octahedral sites, while high-spin Co<sup>2+</sup> (three unpaired  $d$  electrons) occupies tetrahedral sites in an AFM configuration.<sup>81–83</sup> For Mn<sub>3</sub>O<sub>4</sub>, we adopted the “FIM6” configuration, as this was found to be the ground state in previous

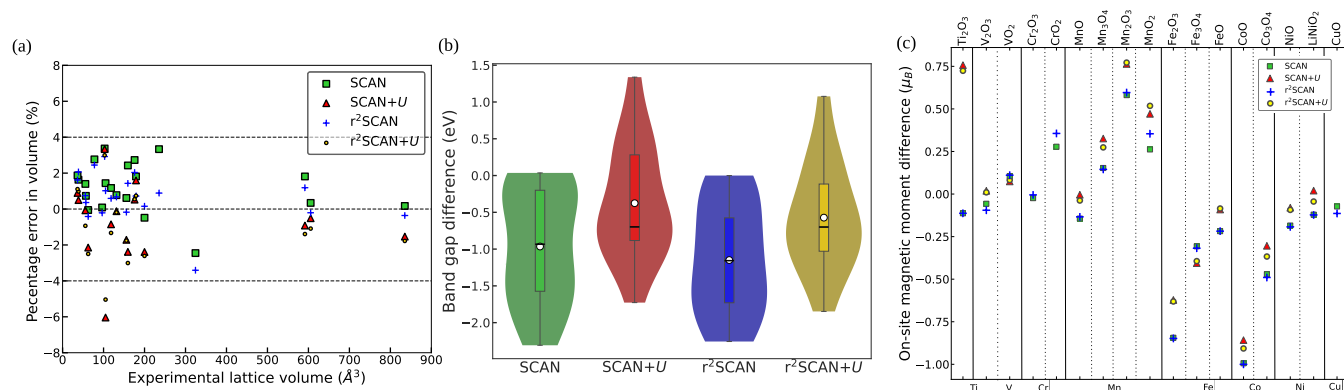


**Figure 2.** (a) Percentage error in volume versus experimental lattice volume (in Å<sup>3</sup>) of all TMOs considered. (b) Violin plot capturing the difference between the experimental and computed band gaps (in eV) across TMO systems using the four XC frameworks. The empty circle and horizontal line in the inner box plot correspond to the mean and median of the calculated band gaps, respectively. (c) Schematic showing the on-site magnetic moment difference between the experimental and calculated values for the TMOs considered. TiO<sub>2</sub>, V<sub>2</sub>O<sub>3</sub>, CrO<sub>3</sub>, and Cu<sub>2</sub>O are not displayed in panel c since their experimental on-site magnetic moments are zero, and all functionals predict the precise experimental value. VO is not included in panel c since its experimental on-site magnetic moment is not known accurately.

work.<sup>38</sup> TiO<sub>2</sub>, CrO<sub>3</sub>, and V<sub>2</sub>O<sub>5</sub> are diamagnetic, since they contain TMs with empty 3*d* orbitals. Similarly, Cu<sub>2</sub>O is diamagnetic owing to the completely filled 3*d* orbitals of Cu.

For calculating the O<sub>2</sub> molecule and the isolated O atom with r<sup>2</sup>SCAN, we considered an asymmetric cell of dimensions 18 Å × 19 Å × 20 Å, in order to capture the triplet ground state electronic configuration of both O<sub>2</sub> and O. We used a total energy convergence criterion of 0.001 meV for both O<sub>2</sub> and O. We initialized the O–O bond distance in the O<sub>2</sub> molecule to the experimental value of 1.21 Å.<sup>84</sup>

**2.3. Determining *U*.** We determined the required *U* value, with r<sup>2</sup>SCAN, for each binary TMO oxidation reaction (e.g., Ti<sup>3+</sup> → Ti<sup>4+</sup> in 2Ti<sub>2</sub>O<sub>3</sub> + O<sub>2</sub> → 4TiO<sub>2</sub>) by comparing the experimental enthalpy (per mole of O<sub>2</sub>) with the calculated (r<sup>2</sup>SCAN+*U*) value that minimizes the error against the experimental value. Note that *U* = 0 eV in our data simply reflects an r<sup>2</sup>SCAN calculation. In order to obtain the experimental oxidation enthalpy, standard enthalpy of formation for all the considered TMOs was taken from the Wagman and/or Kubaschewski tables,<sup>58,60</sup> thus ignoring the *p*–*V* and entropic contributions, similar to previous works.<sup>38,39,85</sup> The overall optimal *U* value for each TM was obtained by taking the average of the required *U* for each of the available oxidation reactions. In the case of Ni oxides, oxidation of NiO to LiNiO<sub>2</sub> by 2Li<sub>2</sub>O + 4NiO + O<sub>2</sub> → 4LiNiO<sub>2</sub> was considered as a proxy for the Ni<sup>2+</sup> → Ni<sup>3+</sup> oxidation reaction.<sup>39</sup>

### 3. RESULTS

**3.1. Oxidation Energetics.** We calculate an oxygen binding energy of ~5.43 eV with r<sup>2</sup>SCAN, which is slightly worse than the SCAN-calculated ~5.15 eV<sup>38</sup> when compared to the experimental ~5.12–5.23 eV.<sup>86,87</sup> However, r<sup>2</sup>SCAN's calculated oxygen binding energy is still significantly better than the estimates by GGA (~5.7–6.2 eV<sup>84,88,89</sup>) or the local density approximation (~7.2–7.6 eV<sup>84,87</sup>). Additionally, previous computational studies have shown r<sup>2</sup>SCAN to exhibit accuracies similar to that of SCAN in predicting formation enthalpies of several main group compounds.<sup>36,37</sup> Moreover, our calculated equilibrium bond length of the O<sub>2</sub> molecule with r<sup>2</sup>SCAN is 1.21 Å, in excellent agreement with both experiment and SCAN calculation.<sup>38,84</sup> Thus, we conclude that

the overbinding of O<sub>2</sub> molecule by r<sup>2</sup>SCAN is quite marginal, and any errors by r<sup>2</sup>SCAN that arise in reaction enthalpies involving TMOs should predominantly be from SIEs involving open-shell *d* electrons.

Figure 1 displays the variation of the enthalpy of different oxidation reactions among binary TMOs, as a function of applied *U* in the r<sup>2</sup>SCAN+*U* framework, for all TMs considered except Cr and Cu. Solid lines in each panel of Figure 1 represent DFT-calculated oxidation enthalpies, with each color corresponding to different oxidation reactions for the TM. For instance in V oxides (Figure 1b), the solid black line corresponds to the oxidation reaction, VO → V<sub>2</sub>O<sub>3</sub>, while the solid red and green lines indicate V<sub>2</sub>O<sub>3</sub> → VO<sub>2</sub> and VO<sub>2</sub> → V<sub>2</sub>O<sub>5</sub>, respectively. Similarly, the experimental enthalpy of each oxidation reaction is represented by a dashed horizontal line of the same color. For example, the black dashed line in Figure 1b indicates the experimental oxidation enthalpy (−7.36 eV) of VO → V<sub>2</sub>O<sub>3</sub>. Also, the dotted vertical line of a given color highlights the required *U* value to minimize the error between DFT-calculated and experimental value for the oxidation reaction enthalpy indicated by the same color. The dotted blue line in each panel signifies the overall optimal *U* for the TM that is averaged across all available oxidation reactions.

We report an optimal *U* value of 2.3, 1.0, 1.8, 3.1, 1.8, and 2.1 eV, respectively, for Ti, V, Mn, Fe, Co, and Ni oxides, within the r<sup>2</sup>SCAN+*U* framework (Figure 1). Notably, the optimal *U* obtained with r<sup>2</sup>SCAN is less than that reported previously for the SCAN functional (Table S1) for all 3*d* TMs considered (except V and Fe), which can be attributed to better accuracy of r<sup>2</sup>SCAN compared to SCAN, as observed in non-TMOs.<sup>36</sup> For V oxides, the required *U* value for VO<sub>2</sub> → V<sub>2</sub>O<sub>3</sub>, V<sub>2</sub>O<sub>3</sub> → VO<sub>2</sub>, VO → V<sub>2</sub>O<sub>3</sub> is 0.0, 0.7, and 2.2 eV, respectively. Thus, the optimal *U* value for V is 1.0 eV (average of the three required *U* values), which is identical to the *U* correction required with SCAN.<sup>39</sup> The decreasing required *U* with increasing oxidation state of V in V oxides is expected due to the decrease in the strength of exchange interactions among the *d* electrons as oxidation state increases. In the case of Fe, FeO → Fe<sub>2</sub>O<sub>3</sub> and FeO → Fe<sub>3</sub>O<sub>4</sub> reactions require a *U* of 2.9 and 3.3 eV, respectively, resulting in an optimal *U* of 3.1 eV, which is also identical to the optimal *U* with SCAN.<sup>38</sup> Moreover, we obtain the highest optimal *U* of 3.1 eV for Fe,

among all TMs considered in this work, which is consistent with the fact that  $\text{Fe}^{3+}$  has the highest number of unpaired  $d$  electrons resulting in the strongest exchange interactions.

For Ti and Ni, we observe a marginal improvement in the  $U$ -value for  $r^2\text{SCAN}$  when compared to SCAN. Specifically, we obtain an optimal  $U$  of 2.3 and 2.1 eV for Ti and Ni, respectively, versus 2.5 eV for both elements with SCAN. We find an optimal  $U$  value of 1.8 eV for both Mn (2.7 eV with SCAN) and Co (3.0 eV with SCAN). In Mn-oxides, the required  $U$  for the oxidation of  $\text{Mn}_2\text{O}_3 \rightarrow \text{MnO}_2$  and  $\text{MnO} \rightarrow \text{Mn}_2\text{O}_3$  is 1.5 and 2.1 eV, respectively. The optimal  $U$  for Mn is transferable to other Mn oxides as well, indicated by the robust agreement between  $r^2\text{SCAN}+U$ -calculated and experimental oxidation enthalpy for  $\text{MnO} \rightarrow \text{Mn}_3\text{O}_4$  (green lines in Figure 1c).

For Cr and Cu oxides, we obtain reasonable agreement with experimental data without a  $U$  correction (Figure S2), similar to our observation with SCAN.<sup>39</sup> In fact, for Cu, introducing  $U$ -correction worsens the error in the calculated oxidation enthalpy for  $\text{Cu}_2\text{O} \rightarrow \text{CuO}$  versus experiment, similar to our observation with SCAN(+ $U$ ) as well, which can be attributed to PAW potentials derived at the PBE-level.<sup>39</sup> However, the magnitude of error (versus experiment) is smaller with  $r^2\text{SCAN}$  ( $\approx 13.1\%$ ) than with SCAN ( $\approx 25.7\%$ ). In the case of Cr, the oxidation reaction of  $\text{CrO}_2 \rightarrow \text{CrO}_3$  requires  $U \sim 0.9$  eV, but introducing a  $U$  correction worsens any agreement with experiment for  $\text{Cr}_2\text{O}_3 \rightarrow \text{CrO}_2$  (where required  $U = 0$  eV). Thus, the optimal  $U$  for Cr oxides is 0.45 eV ( $< 0.5$  eV), which only provides a marginal improvement in describing oxidation enthalpies. Hence, we recommend using only  $r^2\text{SCAN}$  for calculating any Cr oxide framework.

**3.2. Lattice Parameters.** All  $r^2\text{SCAN}(+U)$  and SCAN(+ $U$ ) calculated lattice parameters, on-site magnetic moments, and band gaps for each TMO are tabulated in Table S2. Additionally, the percentage error in the calculated lattice volumes by the four XC functionals is plotted against experimental data in Figure 2a for all oxides. Generally, both SCAN (green squares in Figure 2a) and  $r^2\text{SCAN}$  (blue symbols) offer  $< 4\%$  error in lattice volume compared to the experimental value. Specifically, SCAN and  $r^2\text{SCAN}$  functionals' calculated lattice parameters deviate  $< 2.8\%$  from the experimental lattice parameters for all the TMOs considered, except VO, CuO, and  $\text{LiNiO}_2$ , indicating robust agreement with experiments for both functionals. In VO, SCAN and  $r^2\text{SCAN}$  overestimate (by  $\sim 8\%$ ) the experimental lattice constants, while the deviation in FeO and CuO is  $\sim 3\text{--}4\%$  and  $\sim 8\text{--}10\%$ , respectively. In  $\text{LiNiO}_2$ , SCAN's  $\beta$  angle evaluation is  $\sim 4.1\%$  different from experiment.

Notably, SCAN and  $r^2\text{SCAN}$  do show qualitative differences in their calculated lattice parameters (when compared against experiments) across TMOs. For instance, both functionals overestimate the experimental lattice constants in  $\text{TiO}_2$ ,  $\text{Ti}_2\text{O}_3$ , and VO, while they underestimate in  $\text{CrO}_2$ ,  $\text{CrO}_3$ ,  $\text{MnO}_2$ , and  $\text{Fe}_3\text{O}_4$ . There are also examples ( $\text{MnO}$  and  $\text{Mn}_2\text{O}_3$ ) where SCAN underestimates the experimental lattice constants, while  $r^2\text{SCAN}$  overestimates. Overall, there are cases where SCAN's errors in lattice parameter estimations are lower versus experiments (e.g.,  $\text{Cr}_2\text{O}_3$ , CoO),  $r^2\text{SCAN}$ 's errors are lower (e.g.,  $\text{CrO}_2$ ,  $\text{CrO}_3$ ,  $\text{MnO}_2$ ,  $\text{Fe}_3\text{O}_4$ ), and both functionals exhibit identical errors (e.g.,  $\text{TiO}_2$ ,  $\text{Co}_3\text{O}_4$ , NiO,  $\text{Cu}_2\text{O}$ ), signifying that both functionals offer similar performance in terms of geometrical properties.

Comparing  $r^2\text{SCAN}$  and SCAN, we find that  $r^2\text{SCAN}$ 's lattice constants are generally larger than SCAN across TMOs (e.g.,  $\text{Ti}_2\text{O}_3$ ,  $\text{Cr}_2\text{O}_3$ ,  $\text{CrO}_3$ ,  $\text{VO}_2$ , etc.). As a range,  $r^2\text{SCAN}$  estimates lattice constants that are a maximum of  $\sim 1.5\%$  larger than SCAN (in  $\text{CrO}_3$ ) and a minimum of  $\sim 0.1\%$  larger than SCAN (in  $\text{Mn}_2\text{O}_3$ ). Having said that, there are instances where  $r^2\text{SCAN}$ 's lattice constant evaluations are lower than SCAN (VO, CoO, CuO, and  $\text{LiNiO}_2$ ) and cases where both functionals are identical ( $\text{TiO}_2$ ,  $\text{Co}_3\text{O}_4$ , NiO, and  $\text{Cu}_2\text{O}$ ). In specific TMOs, SCAN and  $r^2\text{SCAN}$  calculate an identical (individual) lattice constant, while the other lattice constants with  $r^2\text{SCAN}$  are larger than SCAN. For example,  $a$  and  $c$  lattice constants with  $r^2\text{SCAN}$  are higher than SCAN in  $\text{V}_2\text{O}_5$ , while both functionals estimate  $b = 3.55 \text{ \AA}$ .

On introducing the optimal  $U$  correction, an increase in the value of calculated lattice constants is obtained for both SCAN and  $r^2\text{SCAN}$  functionals for all TMOs. The lattice constants computed by  $r^2\text{SCAN}+U$  (yellow symbols in Figure 2a) is up to 1.3% higher than  $r^2\text{SCAN}$ , except FeO ( $\sim 4.2\%$  higher). Similar to the comparison of  $r^2\text{SCAN}$  vs SCAN, there are systems where  $r^2\text{SCAN}+U$  predicts larger, smaller, and identical lattice constants compared to SCAN+ $U$  (red triangles). For example,  $r^2\text{SCAN}+U$  calculates larger lattice constants than SCAN+ $U$  in  $\text{VO}_2$ ,  $\text{V}_2\text{O}_5$ , MnO,  $\text{Mn}_2\text{O}_3$  and  $\text{Fe}_3\text{O}_4$  (maximum of  $\sim 0.5\%$  higher in  $\text{V}_2\text{O}_5$ ), while for  $\text{Ti}_2\text{O}_3$ , CoO, and NiO,  $r^2\text{SCAN}+U$ 's estimations are smaller than SCAN+ $U$  (maximum deviation of  $\sim 2.1\%$  in  $\text{Ti}_2\text{O}_3$ ). Both SCAN+ $U$  and  $r^2\text{SCAN}+U$  functionals evaluate identical lattice parameters for  $\text{TiO}_2$ ,  $\text{Co}_3\text{O}_4$ , and  $\text{LiNiO}_2$ .

Overall, lattice constants calculated by SCAN+ $U$  and  $r^2\text{SCAN}+U$  deviate  $< \sim 3.3\%$  from experiments for all TMOs, except VO and  $\text{VO}_2$  where deviations of  $\sim 8.5\%$  and  $\sim 4.6\%$  are observed, respectively. Adding  $U$  improves the agreement with experiment for both SCAN and  $r^2\text{SCAN}$  in  $\text{Co}_3\text{O}_4$ , while  $r^2\text{SCAN}+U$  gives the best estimate of the lattice parameters in FeO ( $< 1\%$  deviation vs experiments) compared to SCAN, SCAN+ $U$ , and  $r^2\text{SCAN}$ . Notably, all functionals break the rocksalt symmetry of VO, MnO, and FeO, while the cubic symmetry of  $\text{Fe}_3\text{O}_4$  is retained only by SCAN. In  $\text{Ti}_2\text{O}_3$ , the hexagonal symmetry is broken by SCAN, but the symmetry is preserved by the other frameworks. In summary, we find that the differences in lattice parameter estimations to be minimal across the four functionals on average, with notable exceptions of a few systems.

**3.3. On-Site Magnetic Moments.** On-site magnetic moments of the TMOs (Figure 2c, see Figure S3 for a heat map representation and Table S2 for the absolute numerical values) computed by SCAN and  $r^2\text{SCAN}$  generally underestimate experimental values, with the exception of  $\text{MnO}_2$ ,  $\text{Mn}_2\text{O}_3$ ,  $\text{CrO}_2$ , and  $\text{VO}_2$ . Note that larger magnetic moments typically indicate stronger localization of  $d$  electrons. Comparing  $r^2\text{SCAN}$  and SCAN calculations, we find that  $r^2\text{SCAN}$  typically estimates smaller magnetic moments than SCAN but with several exceptions, such as MnO,  $\text{MnO}_2$ ,  $\text{Mn}_2\text{O}_3$ ,  $\text{Cr}_2\text{O}_3$ , and  $\text{VO}_2$ . Thus, on average, SCAN's magnetic moment predictions are in better agreement with experiments. However, in terms of magnitude, moments predicted by  $r^2\text{SCAN}$  deviate by  $< 3\%$  from SCAN's estimates, except CuO ( $\sim 6.8\%$  deviation),  $\text{CrO}_2$  ( $\sim 3.5\%$ ), and  $\text{MnO}_2$  ( $\sim 3.5\%$ ), highlighting that the differences in the predictions are marginal.

Adding optimal  $U$  to both SCAN and  $r^2\text{SCAN}$  increases the magnitude of the calculated on-site magnetic moments for all

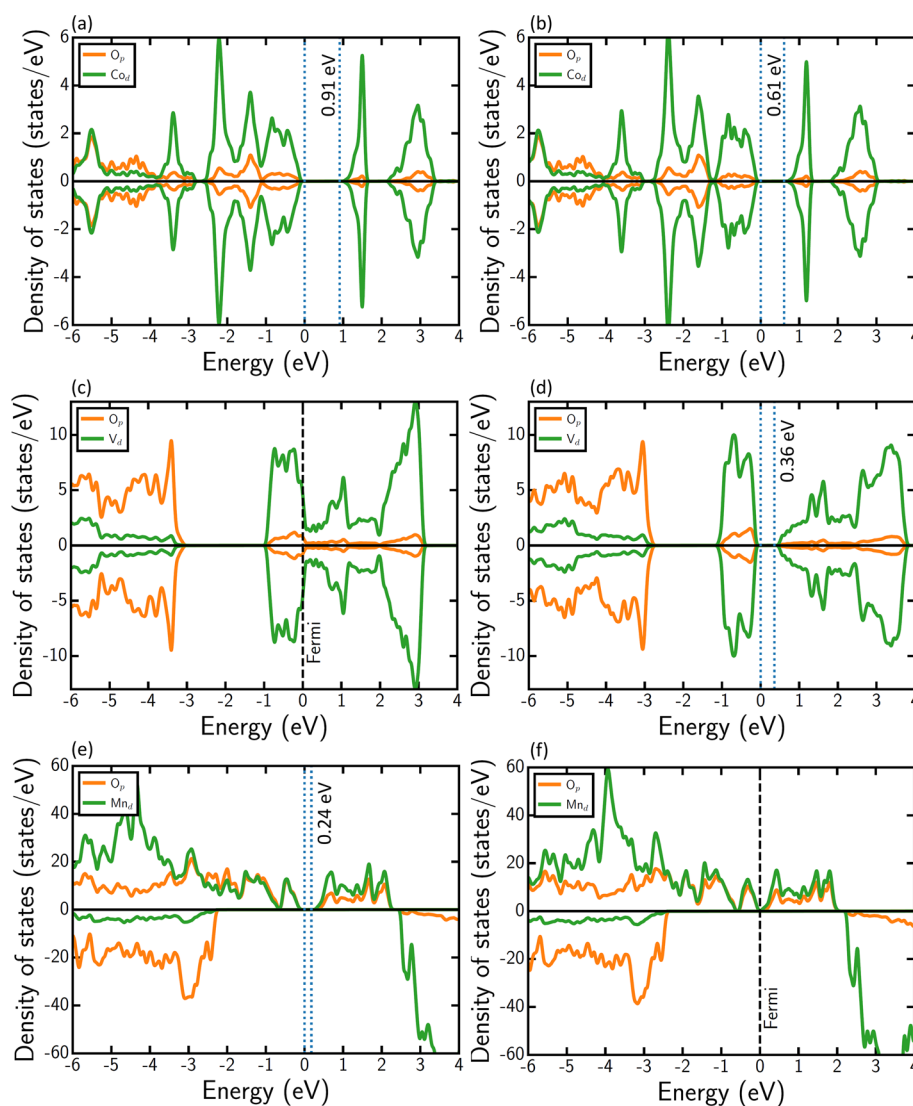


**Figure 3.** DOS for CoO calculated using (a) SCAN and (b)  $r^2$ SCAN, DOS for  $V_2O_3$  computed using (c)  $r^2$ SCAN and (d)  $r^2$ SCAN+ $U$ , and DOS for  $Mn_2O_3$  estimated using (e) SCAN+ $U$  and (f)  $r^2$ SCAN+ $U$ .

TMOs (except  $VO_2$ , which is predicted to be metallic by all functionals), consistent with the expectation that the  $U$  correction facilitates  $d$  electron localization.  $r^2$ SCAN+ $U$ -calculated data are similar to the corresponding SCAN+ $U$  values (<2.3% variation), except for  $LiNiO_2$  (~6.3% variation) and  $Ti_2O_3$  (~3.8%). Similar to  $r^2$ SCAN versus SCAN,  $r^2$ SCAN+ $U$  estimates smaller magnetic moments than SCAN+ $U$ , with notable exceptions being  $VO_2$ ,  $Mn_2O_3$ ,  $MnO_2$ , and  $FeO$ . Overall, we observe the accuracy in calculated on-site magnetic moments versus experiments to follow the order SCAN+ $U$  >  $r^2$ SCAN+ $U$  > SCAN >  $r^2$ SCAN for several TMOs. However, there are specific cases where specific XC frameworks offer better accuracy in calculating magnetic moments, such as SCAN in  $CrO_2$ ,  $Mn_2O_3$ ,  $MnO_2$ ,  $Fe_3O_4$ , and  $CuO$ ,  $r^2$ SCAN in  $Mn_3O_4$  and  $Cr_2O_3$ , and  $r^2$ SCAN+ $U$  in  $V_2O_3$ . Given the numerically marginal deviations in calculated magnetic moments across the XC frameworks (~10% deviation), we expect an increase/decrease in accuracy to be marginal among the XC frameworks considered.

**3.4. Band Gaps.** The differences between calculated and experimental band gaps of all TMOs considered are visualized as violin plots for SCAN (green violin), SCAN+ $U$  (red),

$r^2$ SCAN (blue), and  $r^2$ SCAN+ $U$  in Figure 2b. The top and bottom ends of the individual violins mark the highest and lowest differences in the respective calculated data. Note that the mean values (white empty circles) are similar for SCAN and  $r^2$ SCAN and, in turn, lower than their  $U$ -corrected versions. In other words, addition of the  $U$ -correction reduces the error of calculated band gaps compared to experimental values, which is expected given that semilocal DFT typically underestimates band gaps. Also, we find that SCAN+ $U$  displays the lowest mean band gap difference among the XC functionals considered, indicating that on-average SCAN+ $U$  provides better computed band gaps.

We present calculated electronic DOS of select TMOs, namely CoO (panels a and b),  $V_2O_3$  (c and d), and  $Mn_2O_3$  (e and f), in Figure 3, to illustrate qualitative trends in computed band gaps. The DOS for the remaining TMOs, calculated by the four XC frameworks, are compiled in Figures S5–S21 of the SI. In each DOS panel, solid orange and solid green lines correspond to the  $2p$ -states of O and the  $3d$ -states of the TM, respectively. Dashed black lines represent Fermi levels in metallic compounds. Dotted vertical lines represent valence and conduction band edges in semiconducting/insulating

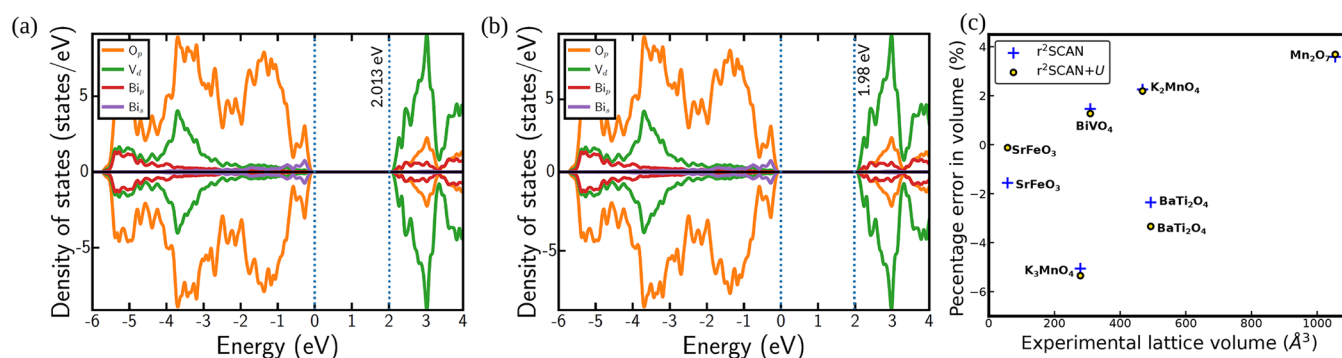


**Figure 4.** DOS for  $\text{BiVO}_4$  calculated using (a)  $r^2\text{SCAN}$  and (b)  $r^2\text{SCAN}+U$ . (c) Percentage error in calculated volume versus experimental lattice volume (in  $\text{\AA}^3$ ) using  $r^2\text{SCAN}$  and  $r^2\text{SCAN}+U$  for various structures that are indicated by text annotations.

compounds, with the band gaps indicated by the text annotation near the conduction band minimum (CBM). The zero of the energy scale is set to the valence band maximum (VBM) for TMOs with a band gap and to the Fermi level in metallic TMOs.

We observe that  $r^2\text{SCAN}$  generally calculates a smaller band gap than SCAN for most TMOs (maximum of  $\sim 66\%$  lower in  $\text{MnO}_2$ , see Table S2), as illustrated by the case of  $\text{CoO}$  in panels a and b of Figure 3. Notable exceptions do exist for this observation, such as  $\text{V}_2\text{O}_5$  ( $\sim 1.7\%$  larger),  $\text{CrO}_3$  ( $\sim 3.2\%$ ),  $\text{MnO}$  ( $\sim 4.3\%$ ), and  $\text{Fe}_2\text{O}_3$  ( $\sim 1.7\%$ ), where  $r^2\text{SCAN}$  calculated band gaps are marginally larger than SCAN. Both SCAN and  $r^2\text{SCAN}$  incorrectly describe the ground state electronic configuration of narrow band gap TMOs (i.e., experimental band gaps  $< 1$  eV), including  $\text{Ti}_2\text{O}_3$  (Figure S6),  $\text{V}_2\text{O}_3$  (Figure 3c and S5c),  $\text{VO}_2$  (Figure S9), and  $\text{Fe}_3\text{O}_4$  (Figure S17) to be metallic, with the exception of  $\text{MnO}_2$  where both SCAN and  $r^2\text{SCAN}$  estimate a narrow gap (Figures S14a and S14c). Additionally, both functionals also calculate the wrong electronic structure in the case of a non-narrow-gap semiconductor,  $\text{Mn}_2\text{O}_3$  (Figure S5), which exhibits an experimental gap of 1.2–1.3 eV.<sup>90,91</sup> However, SCAN and  $r^2\text{SCAN}$  qualitatively describe the right electronic structure in the case of wide band gap TMOs such as  $\text{FeO}$  (Figure S15),  $\text{Fe}_2\text{O}_3$  (Figure S16), and  $\text{NiO}$  (Figure S19), with a significant quantitative underestimation of the experimental gaps. In any case, the differences in electronic structure predictions between SCAN and  $r^2\text{SCAN}$  in TMOs are minimal, with SCAN being marginally better in accuracy.

Introducing a  $U$  correction to SCAN and  $r^2\text{SCAN}$  widens or opens the band gap, especially in narrow band gap TMOs, as illustrated by the case of  $\text{V}_2\text{O}_3$  (panels c and d in Figure 3). The opening of the band gap with  $U$  correction is expected since localization of  $d$  electrons, which form the VBM and/or CBM in  $3d$ -TMOs, is facilitated with  $U$  addition, in turn resulting in a larger gap. However, in the case of  $\text{VO}_2$  (Figure S9), adding  $U$  does not capture the MIT that occurs at low temperatures ( $< 341$  K<sup>63</sup>) with either SCAN or  $r^2\text{SCAN}$ , causing the erroneous prediction of metallic behavior. Generally, SCAN+ $U$  calculates a larger band gap than  $r^2\text{SCAN}+U$  (Table S2), as highlighted by the case of  $\text{Mn}_2\text{O}_3$  (panels e and f in Figure 3). In fact, SCAN+ $U$  is the only framework (among those considered) to estimate a band gap in  $\text{Mn}_2\text{O}_3$ , which is consistent with experiment. Moreover, SCAN+ $U$ 's evaluations of larger band gaps result in better (poorer) quantitative agreement with experiments in wide

(narrow) gap materials, such as  $\text{MnO}$  and  $\text{FeO}$  ( $\text{V}_2\text{O}_3$  and  $\text{MnO}_2$ ).

Note that SCAN+ $U$  and  $r^2\text{SCAN}+U$  do underestimate the experimental band gaps, similar to SCAN and  $r^2\text{SCAN}$ , in wide gap TMOs. The only exception to this observation is  $\text{CoO}$ , where SCAN+ $U$  overestimates the band gap versus experiment (Figure S5a and Table S2), as also observed in our previous work.<sup>39</sup> In select TMOs, including  $\text{Fe}_2\text{O}_3$  and  $\text{V}_2\text{O}_5$ ,  $r^2\text{SCAN}+U$ 's band gap is larger than SCAN+ $U$ , but the magnitude of difference ( $\leq 0.2$  eV) is meager. Thus, for electronic structure predictions, we expect SCAN+ $U$  to provide the best qualitative and quantitative band gaps across TMOs, among the functionals considered here, especially for wide gap semiconductors/insulators. However, the qualitative trends provided by  $r^2\text{SCAN}+U$  are quite robust as well, and in small gap semiconductors ( $< 1$  eV gap),  $r^2\text{SCAN}+U$ 's quantitative accuracy is often better than SCAN+ $U$ .

**3.5. Transferability Checks.** To examine the transferability of the optimal  $U$  values determined in this work (with  $r^2\text{SCAN}$ ), to oxide systems not used for obtaining the values, we perform checks on systems with different oxidation states and/or coordination environments for each TM. We compare calculated values against available experimental data, such as structural, electronic, magnetic, and/or electrochemical properties. Specifically, we choose  $\text{Ba}_2\text{TiO}_4$  as a check for Ti,  $\text{BiVO}_4$  for V,  $\text{K}_3\text{MnO}_4$ ,  $\text{K}_2\text{MnO}_4$ , and  $\text{Mn}_2\text{O}_7$  for Mn,  $\text{SrFeO}_3$  for Fe,  $\text{LiCoO}_2$ – $\text{CoO}_2$  for Co, and  $\text{LiNiO}_2$ – $\text{NiO}_2$  for Ni. Data related to transferability checks are compiled in Figure 4, Table 1, Table S3, and Figure S4.

In the case of  $\text{Ba}_2\text{TiO}_4$ , we compare the calculated lattice parameters with experimental values (percentage error in calculated volumes plotted in Figure 4, see Table S3 for the absolute values).  $\text{Ba}_2\text{TiO}_4$  crystallizes in a monoclinic structure (space group  $P2_1/n$ ) at low temperatures, where the unit cell is composed of four formula units.<sup>92,93</sup> Ti atoms are present in distorted tetrahedra composed of neighboring oxygen atoms ( $\text{TiO}_4$ ) within the  $\text{Ba}_2\text{TiO}_4$  lattice, which is different from the octahedral environments sampled in  $\text{TiO}_2$  and  $\text{Ti}_2\text{O}_3$ . Upon structure relaxation, we observe that both  $r^2\text{SCAN}$  and  $r^2\text{SCAN}+U$  functionals marginally overestimate (by  $\sim 2\%$ ) experimental lattice parameters (Figure 4 and Table S3). Similar to trends observed in Table S2, adding  $U$  to  $r^2\text{SCAN}$  increases the calculated lattice parameters in  $\text{Ba}_2\text{TiO}_4$  (by  $\sim 0.03$   $\text{\AA}$ ), thereby marginally reducing the agreement with experiment.

We benchmark both structural and electronic properties of  $\text{BiVO}_4$  as a transferability check for V-based systems. Note that

**Table 1. Voltage and Magnetic Moments Calculated by  $r^2$ SCAN and  $r^2$ SCAN+ $U$  Compared against Experimental Values<sup>a</sup>**

| Composition (space group)                            | Source          | Voltage (V) | Magnetic moment ( $\mu_B$ ) |
|--|-----------------|-------------|-----------------------------|
| LiCoO <sub>2</sub> –CoO <sub>2</sub> ( $R\bar{3}m$ ) | Expt.           | 4.05        | -                           |
|  | $r^2$ SCAN      | 4.12        | -                           |
|  | $r^2$ SCAN+ $U$ | 4.23        | -                           |
| LiNiO <sub>2</sub> –NiO <sub>2</sub> ( $P1m1$ )      | Expt.           | 3.85        | -                           |
|  | $r^2$ SCAN      | 3.54        | -                           |
|  | $r^2$ SCAN+ $U$ | 3.92        | -                           |
| SrFeO <sub>3</sub> ( $Pm\bar{3}m$ )                  | Expt.           | -           | $2.7 \pm 0.4$               |
|  | $r^2$ SCAN      | -           | 3.375                       |
|  | $r^2$ SCAN+ $U$ | -           | 3.819                       |

<sup>a</sup>Denoted by ‘Expt.’. The  $U$  values used with  $r^2$ SCAN+ $U$  are the corresponding optimal  $U$  values obtained for each TM (from Figure 1).

BiVO<sub>4</sub> transforms from tetragonal ( $I41/a$ ) to a monoclinic ( $I2/b$ ) “scheelite” phase below  $\sim 528$  K,<sup>94,95</sup> which is a reversible second order ferroelastic transition driven by soft optical phonon modes. The BiVO<sub>4</sub> unit cell possesses four formula units, with tetrahedrally coordinated V ions, which is different from the coordination environments of V in VO, V<sub>2</sub>O<sub>3</sub>, VO<sub>2</sub>, and V<sub>2</sub>O<sub>5</sub>. Importantly, monoclinic-BiVO<sub>4</sub> spontaneously transforms to the tetragonal structure upon structure relaxation with  $r^2$ SCAN and  $r^2$ SCAN+ $U$ , similar to the observation by Liu et al.<sup>94</sup> with GGA and hybrid functionals. Thus, neither  $r^2$ SCAN nor  $r^2$ SCAN+ $U$  predict the correct ground state structure. Additionally, BiVO<sub>4</sub> possesses a band gap of 2.4–2.48 eV<sup>96</sup> and is a candidate photocatalyst.<sup>94</sup> Both  $r^2$ SCAN and  $r^2$ SCAN+ $U$  provide similar band gap predictions (2.01–1.98 eV), which is in good qualitative agreement with experiment. Surprisingly,  $r^2$ SCAN+ $U$  evaluates a marginally lower band gap than  $r^2$ SCAN (see panels a and b in Figure 4). However, both  $r^2$ SCAN and  $r^2$ SCAN+ $U$  predict similar states occupying the valence band ( $O_p$ ) and conduction band ( $V_d$ ) edges.

The rationale behind the choice of K<sub>3</sub>MnO<sub>4</sub>, K<sub>2</sub>MnO<sub>4</sub>, and Mn<sub>2</sub>O<sub>7</sub> as checks for Mn-based systems is to explore the higher, unsampled oxidation states of Mn, namely +5, +6, and +7, in K<sub>3</sub>MnO<sub>4</sub>, K<sub>2</sub>MnO<sub>4</sub>, and Mn<sub>2</sub>O<sub>7</sub>, respectively. Also, Mn resides in tetrahedral coordination in these compounds, which is different from the octahedral coordination observed in MnO, Mn<sub>2</sub>O<sub>3</sub>, and MnO<sub>2</sub>. Although Mn<sup>2+</sup> resides in tetrahedral sites in spinel-Mn<sub>3</sub>O<sub>4</sub>, we had not used it in the spinel structure to obtain our optimal  $U$ . We benchmark the calculated lattice parameters versus experiments for all Mn-based transferability checks.

Mn<sub>2</sub>O<sub>7</sub> is a volatile liquid at 298 K and solidifies to a monoclinic crystal structure ( $P2_1/c$ ) below  $\sim 279$  K, with the unit cell consisting of 8 formula units of corner sharing tetrahedral MnO<sub>4</sub> pairs.<sup>97,98</sup> Upon structural relaxation, both  $r^2$ SCAN and  $r^2$ SCAN+ $U$  underestimate the lattice constants of monoclinic-Mn<sub>2</sub>O<sub>7</sub> by  $\sim 1$ –3% (Figure 4 and Table S3). In the case of K<sub>3</sub>MnO<sub>4</sub>, the tetragonal symmetry ( $I\bar{4}2m$ )<sup>99</sup> is broken with the  $r^2$ SCAN functional resulting in an orthorhombic structure, while the symmetry is preserved by  $r^2$ SCAN+ $U$  (see Figure 4 and Table S3). Nonetheless, both  $r^2$ SCAN and  $r^2$ SCAN+ $U$  significantly underestimate the  $c$  parameter (by  $\sim 13.5\%$ ) and overestimate the  $a$  or  $b$  parameter ( $\sim 10.2\%$ ). K<sub>2</sub>MnO<sub>4</sub> is an orthorhombic crystal ( $Pnma$ ) with four formula

units per unit cell.<sup>100</sup> Here,  $r^2$ SCAN and  $r^2$ SCAN+ $U$  predict identical lattice parameters, which marginally underestimate experimental values (by  $\sim 0.4$ –1%, see Figure 4 and Table S3).

The choice of SrFeO<sub>3</sub>, a cubic perovskite, as a check for Fe is largely motivated by the 4+ oxidation state exhibited by Fe in the structure, which is not sampled in FeO, Fe<sub>2</sub>O<sub>3</sub>, or Fe<sub>3</sub>O<sub>4</sub>. Both  $r^2$ SCAN and  $r^2$ SCAN+ $U$  preserve the cubic symmetry during structure relaxation, with  $r^2$ SCAN+ $U$ 's lattice parameters identical to experiments and  $r^2$ SCAN's parameters being a slight underestimation ( $\sim 0.5\%$ , see Figure 4 and Table S3). In terms of the magnetic configuration of Fe in SrFeO<sub>3</sub>, Takeda et al.<sup>101</sup> reported a helical spin structure via their neutron diffraction experiments, with competing FM and AFM interactions. However, Shein et al.<sup>102</sup> found an FM metallic state to be the ground state of SrFeO<sub>3</sub>, over a wide range of pressures, based on their first-principles calculations, which they attributed to stronger FM than AFM interactions. We considered an FM configuration of Fe atoms in the SrFeO<sub>3</sub> unit cell, and the on-site magnetic moments on Fe calculated by both  $r^2$ SCAN (3.375  $\mu_B$ , Table 1) and  $r^2$ SCAN+ $U$  (3.819  $\mu_B$ ) overestimate the experimental value ( $2.7 \pm 0.4$   $\mu_B$ <sup>101</sup>). However, our calculated magnetic moments do indicate a localization of  $\sim 4$  electrons on the  $d$  orbitals of Fe, consistent with its +4 oxidation state.

We choose CoO<sub>2</sub> ( $R\bar{3}m$  or the ‘O3’ polymorph<sup>103</sup>) and NiO<sub>2</sub> ( $P1m1$  or ‘O1’<sup>104</sup>), both layered structures, as transferability checks for Co and Ni, respectively, owing to the unsampled 4+ oxidation states of each TM. In terms of experimental property to benchmark, we choose the average Li intercalation voltage in these structures, i.e., LiCoO<sub>2</sub>–CoO<sub>2</sub> and LiNiO<sub>2</sub>–NiO<sub>2</sub> pairs, since they have been measured with high precision. The reader is referred to previous works on calculating and benchmarking average “topotactic” intercalation voltages.<sup>105,106</sup>  $r^2$ SCAN underestimates the experimental average voltage<sup>103,106–110</sup> in LiNiO<sub>2</sub>–NiO<sub>2</sub> (by  $\sim 8\%$ ), while it overestimates the average voltage in LiCoO<sub>2</sub>–CoO<sub>2</sub> (by  $\sim 1.7\%$ ), similar to trends observed with SCAN.<sup>106</sup> The addition of  $U$  to  $r^2$ SCAN leads to an improvement in agreement with the experimental voltage in the Ni-system (deviation of  $\sim 1.8\%$ ), while it worsens the agreement in the Co-system (deviation of  $\sim 4.4\%$ ). Nevertheless,  $r^2$ SCAN+ $U$  does overestimate the average voltage in both Co and Ni systems, similar to the behavior of SCAN+ $U$ .<sup>106</sup>

## 4. DISCUSSION

In this work, we evaluated the performance of the  $r^2$ SCAN functional among binary TMOs consisting of 3d-TMs by calculating the oxidation enthalpies, lattice parameters, on-site magnetic moments, and band gaps. Additionally, for each TM-O<sub>2</sub> system considered, we calculated the optimal Hubbard- $U$  corrections to be used in an  $r^2$ SCAN+ $U$  framework, based on experimental oxidation enthalpies. Although theoretical approaches exist to derive  $U$  values,<sup>42–48</sup> using oxidation enthalpies nominally gives an “average” correction that is suitable across several oxidation states of a given TM. Specifically, our optimal  $U$  values are 2.3, 1.0, 1.8, 3.1, 1.8, and 2.1 eV for Ti, V, Mn, Fe, Co, and Ni, respectively, while we do not deem a  $U$  correction necessary for Cr and Cu oxides. Interestingly, the optimal  $U$  corrections needed with  $r^2$ SCAN are lower in magnitude compared to SCAN for Ti, Mn, Co, and Ni oxides (while the corrections are identical for V and Fe oxides), indicating that  $r^2$ SCAN exhibits lower errors with oxidation enthalpies and possibly lower SIEs than SCAN.



However, this is not reflected in other physical properties. On average, we find the accuracy, versus experimental values, to be similar for  $r^2$ SCAN compared to SCAN and for  $r^2$ SCAN+ $U$  compared to SCAN+ $U$ , respectively, in lattice parameter, on-site magnetic moment, and band gap evaluations as seen in Figure 2.

The general trends in lattice parameter, magnetic moment, and band gap predictions, across the XC frameworks considered, can be summarized as follows. We observe that  $r^2$ SCAN generates larger lattice constants than SCAN, and on addition of the  $U$  correction to both functionals, the lattice constants further increase. Thus, in systems where SCAN underestimates experimental lattice constants (e.g.,  $\text{CrO}_2$ ,  $\text{CrO}_3$ ,  $\text{MnO}_2$ ), shifting to  $r^2$ SCAN improves agreement (e.g., error in  $r^2$ SCAN in  $\text{CrO}_3$  is 0.8% versus 2.3% with SCAN). Also, there are instances where the ground state symmetry of the TMO is not preserved by some or all of the XC frameworks considered (i.e., in VO, MnO, FeO,  $\text{Fe}_3\text{O}_4$ , and  $\text{Ti}_2\text{O}_3$ ), highlighting systematic issues in the XC treatment across the four frameworks considered. The calculated on-site magnetic moments by  $r^2$ SCAN (and  $r^2$ SCAN+ $U$ ) are marginally lower than SCAN (SCAN+ $U$ ), with the  $U$  correction nominally increasing the calculated moments calculated by  $r^2$ SCAN and SCAN. However, calculated magnetic moments across the four XC frameworks differ by <10% (except  $\text{LiNiO}_2$ ), signifying marginal differences in accuracy. Both SCAN and  $r^2$ SCAN underestimate band gaps across all TMOs (except  $\text{MnO}_2$ ), with band gaps calculated by  $r^2$ SCAN typically being lower than SCAN, and adding the  $U$  opens/widens the gap. Thus, SCAN+ $U$  offers the best quantitative accuracy versus experimental band gaps, especially for wide gap semiconductors. Note that the qualitative trends from  $r^2$ SCAN+ $U$  are consistent with the trends exhibited by SCAN+ $U$  and should be reliable in electronic structure predictions in other TM-based oxide systems.

$r^2$ SCAN adopts the smooth polynomial interpolation function of  $r$ SCAN to maintain numerical stability during SCF calculations. Additionally, the reformed gradient expansion for correlation introduced in  $r^2$ SCAN (partially) negates the error introduced to the slowly varying density by the nonvanishing interpolation function,<sup>32</sup> which largely accounts for the observed variation in accuracy of  $r^2$ SCAN versus SCAN. Based on our data, we observe that  $r^2$ SCAN is not systematically more accurate than SCAN across all TMOs and for all property predictions. For example, we have not only lower optimal  $U$  values indicating lower SIEs with  $r^2$ SCAN versus SCAN but also lower on-site magnetic moments (except Mn and Cr oxides) signifying poorer  $d$ -electron localization with  $r^2$ SCAN. Further, the smaller band gaps with  $r^2$ SCAN (versus SCAN) may be caused by the residual SIEs, resulting in an underestimation of the CBM across TMOs. Hence, usage of  $r^2$ SCAN(+ $U$ ) in TM-based systems must be done with care, and efforts should be made to benchmark as many available experimental properties as possible before performing “true” computational predictions.

We note that the impact of adding  $U$  on oxidation enthalpy changes is different for different TMs, similar to trends observed with SCAN+ $U$  as well.<sup>38,39</sup> For example, in Ti-oxides, adding a  $U = 2.5$  eV causes a variation in oxidation enthalpy of  $\sim 0.9$  eV (Figure 1a), while a similar addition in Co-oxides causes a change of  $\sim 3$  eV (Figure 1e). Apart from the number of  $d$  electrons involved within the reactant or product of a given reaction (and consequently the SIEs contributed), the

sensitivity of oxidation enthalpy with  $U$  in a given TM- $\text{O}_2$  system is also dictated by the total oxidation state change in a given reaction. For instance, reactions involving smaller oxidation state changes (such as  $\text{FeO} \rightarrow \text{Fe}_3\text{O}_4$  or  $\text{Fe}^{2+} \rightarrow \text{Fe}^{2.67+}$ , Figure 1d) exhibit larger changes in their oxidation enthalpies with  $U$  than reactions involving larger oxidation state changes (such as  $\text{FeO} \rightarrow \text{Fe}_2\text{O}_3$ ). This is primarily because, our oxidation enthalpies are normalized per  $\text{O}_2$  and not per number of electrons transferred. The one exception to this trend is  $\text{MnO} \rightarrow \text{Mn}_3\text{O}_4$  that exhibits similar slopes of oxidation enthalpy versus  $U$  compared to  $\text{MnO} \rightarrow \text{Mn}_2\text{O}_3$  and  $\text{Mn}_2\text{O}_3 \rightarrow \text{Mn}_3\text{O}_4$ , which can be attributed to the presence of the Jahn–Teller-active  $\text{Mn}^{3+}$  oxidation state in  $\text{Mn}_2\text{O}_3$ .

In the case of  $\text{Ti}_2\text{O}_3 \rightarrow \text{TiO}_2$ , the nonmonotonic variation of the oxidation enthalpy with + $U$  is largely because of improper localization of the sole  $d$  electron in  $\text{Ti}_2\text{O}_3$  (Figure 1a). For instance, adding  $U = 1$  eV gives rise to an on-site magnetic moment of  $\sim 0.61 \mu_B$  which is a semidelocalized valence electronic configuration in  $\text{Ti}_2\text{O}_3$ , while adding  $U = 2$  eV gives rise to a better on-site magnetic moment of  $\sim 0.85 \mu_B$  indicating a better localized electronic state. Note that the total energy of a given system with delocalized electrons is penalised more (i.e., becomes more positive) with  $U$  addition than without it. Consequently, the oxidation enthalpy is lower at  $U = 1$  eV for  $\text{Ti}_2\text{O}_3 \rightarrow \text{TiO}_2$  compared to  $U = 0$  and 2 eV, since the total energy of  $\text{Ti}_2\text{O}_3$  is underestimated by  $r^2$ SCAN+ $U$  at  $U = 1$  eV. Note that we observe a similar nonmonotonic trend of oxidation enthalpy change versus  $U$  for the Ti– $\text{O}_2$  system with SCAN+ $U$  as well.<sup>39</sup>

We considered the transferability of the  $U$  values estimated in this work, with  $r^2$ SCAN, by examining systems for each TM with oxidation states and/or coordination environments not sampled while calculating the optimal  $U$ . In general, we find that  $r^2$ SCAN or its Hubbard  $U$  corrected version estimates similar lattice parameters and hence yields similar accuracies on structural properties. Analogously, the calculated on-site magnetic moments in  $\text{SrFeO}_3$  and the band gaps in  $\text{BiVO}_4$  are similar between  $r^2$ SCAN and  $r^2$ SCAN+ $U$ .

In the case of electrochemical properties, we do find tangible variations in the calculated average voltages of  $r^2$ SCAN and  $r^2$ SCAN+ $U$ , with  $r^2$ SCAN+ $U$  exhibiting lower error in the Ni system. We note that  $r^2$ SCAN provides a more accurate average Li-intercalation voltage in  $\text{CoO}_2$  (4.12 V) compared to experiment (4.05 V) than  $r^2$ SCAN+ $U$  (4.23 V, Table 1). However, the lower errors of  $r^2$ SCAN in predicting voltage is likely due to lower SIEs arising out of low-spin configurations of  $\text{Co}^{3+}$  and  $\text{Co}^{4+}$  in  $\text{LiCoO}_2$  and  $\text{CoO}_2$ , respectively. Given that  $r^2$ SCAN does make significant errors in oxidation enthalpies involving high-spin  $\text{Co}^{2+}$  ions in  $\text{CoO-Co}_3\text{O}_4$  (Figure 1e) and that  $r^2$ SCAN+ $U$  makes a reasonable voltage prediction, we expect our  $U$  to be an optimal choice, particularly for modeling a wide range of oxidation states and high-spin configurations of Co. Overall, we find the optimal  $U$  values obtained in this work to be transferable across oxide frameworks not sampled *a priori*. Nevertheless, more benchmarking studies to compare the performance of  $r^2$ SCAN+ $U$  with  $r^2$ SCAN (and experiments) will help in quantifying the reliability and errors associated with using  $r^2$ SCAN+ $U$  for a wide variety of applications.

Given that  $r^2$ SCAN(+ $U$ ) is not systematically more or less accurate than SCAN(+ $U$ ), the computational performance and numerical stability of  $r^2$ SCAN(+ $U$ ) is critical in determining its utility in property predictions across materials. Thus, we have

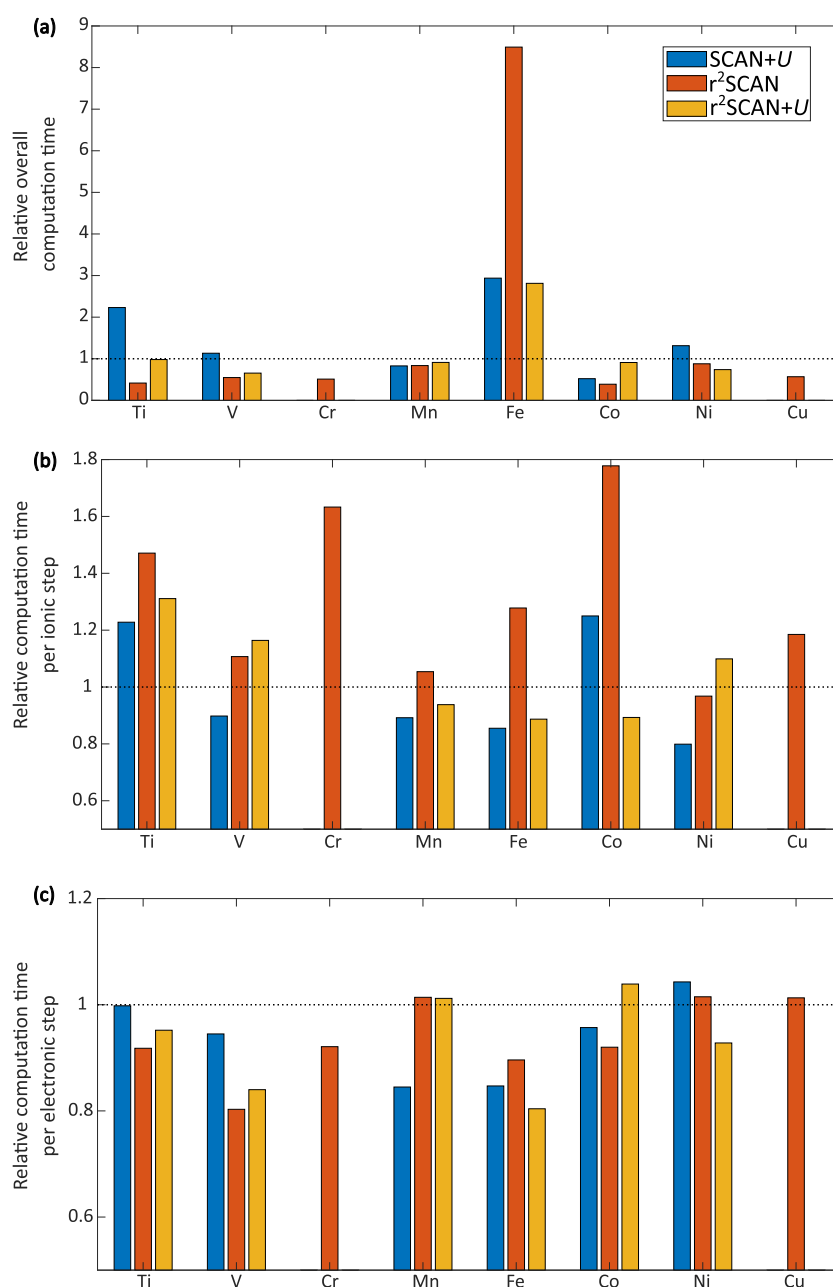


**Figure 5.** (a) Overall computational time (electronic+ionic steps), (b) computational time per ionic step, and (c) computational time per electronic loop taken for each TM-O<sub>2</sub> binary system with SCAN+U, r<sup>2</sup>SCAN, and r<sup>2</sup>SCAN+U frameworks relative to SCAN. Values greater (smaller) than 1 in each panel indicate that a given calculation is slower (faster) than SCAN.

quantified the computational time of r<sup>2</sup>SCAN(+U) and SCAN+U relative to SCAN for each TM-O<sub>2</sub> system considered in Figure S1. Specifically, panels a, b, and c of Figure 5 plot the overall (electronic+ionic steps), per ionic step, and per electronic step computational time, respectively, taken by the SCAN+U (blue bars), r<sup>2</sup>SCAN (red), and r<sup>2</sup>SCAN+U (yellow) frameworks, relative to the computational time taken by the SCAN functional (dotted black lines), for each TM-based set of oxides. Details on calculating the computational times used by the functionals is described in the “Computational time” section of the SI. Note that our objective is not to provide a rigorous quantification of computational resources required for each XC framework but to provide a qualitative understanding of the relative computational costs across the frameworks considered.

For each electronic step, r<sup>2</sup>SCAN(+U) is typically faster than SCAN (Figure 5), signifying better numerical stability than SCAN, with Mn, Ni, and Cu oxides being marginal exceptions. In contrast, on a per-ionic step basis, r<sup>2</sup>SCAN and r<sup>2</sup>SCAN+U are slower than SCAN, by ~1.05–1.78× and ~1.1–1.31×, respectively, highlighting that r<sup>2</sup>SCAN(+U) takes more electronic steps to converge per ionic step. Importantly, the overall computational time (ionic+electronic steps, Figure 5) required for structural relaxation of TMOs using r<sup>2</sup>SCAN and r<sup>2</sup>SCAN+U is lower than SCAN, by ~12.1–61.2% and ~1.9–34.5%, respectively, except in Fe oxides, indicating that r<sup>2</sup>SCAN(+U) takes a lower number of ionic steps to converge, which possibly indicates a better description of atomic forces. The higher overall computation time in Fe oxides with r<sup>2</sup>SCAN(+U) than SCAN is primarily due to the difficulty in

converging  $\text{Fe}_3\text{O}_4$  with  $r^2\text{SCAN}(+U)$ . Comparing  $r^2\text{SCAN}$  and  $r^2\text{SCAN}+U$ , we find that  $r^2\text{SCAN}+U$  takes a higher overall computational time to converge, except in Fe and Ni oxides. Thus, we expect  $r^2\text{SCAN}(+U)$  to provide good utility in property predictions in TM-containing systems given its better computational performance and reasonable accuracy compared to  $\text{SCAN}(+U)$ .

## 5. CONCLUSION

3d-TMs and their compound phases find applications in several fields such as energy storage, solar cells, catalysts, thermochemical water splitting, etc., and it is imperative to predict their properties such as lattice constants, magnetic moments, reaction enthalpies, and band gaps accurately using DFT-based techniques for designing better materials. Recently, the  $r^2\text{SCAN}$  metaGGA XC functional was proposed to exhibit the accuracy of its predecessor, SCAN, and the computational performance of  $r^2\text{SCAN}$  in main-group compounds, but the accuracy of  $r^2\text{SCAN}$  was not rigorously tested on TM-based systems. Here, we assessed the numerical accuracy and computational performance of  $r^2\text{SCAN}$  in binary 3d-TMOs, in calculating the lattice parameters, on-site magnetic moments, binary oxidation enthalpies, and band gaps against experimental data. Notably, we observed that  $r^2\text{SCAN}$  exhibited similar qualitative trends as that of SCAN, with marginally larger estimations of lattice parameters than SCAN, while the on-site magnetic moments and band gap calculations are marginally smaller than SCAN. While both  $r^2\text{SCAN}$  and SCAN underestimated the band gaps in wide gap TMOs, with SCAN offering slightly better accuracy, they failed to predict the correct ground state electronic configurations of narrow band gap TMOs (e.g.,  $\text{Mn}_2\text{O}_3$ ).

On analyzing the addition of Hubbard  $U$ -correction to improve the accuracy of the  $r^2\text{SCAN}$  functional, we observed that a lower optimal  $U$  value, based on experimental oxidation enthalpies, was required in an  $r^2\text{SCAN}+U$  framework for Ti, Mn, Co, and Ni oxides, when compared to a  $\text{SCAN}+U$  framework. The optimal  $U$  values were identical in both  $r^2\text{SCAN}+U$  and  $\text{SCAN}+U$  frameworks for V and Fe oxides, while we did not observe the need for a  $U$  correction in Cr and Cu oxides with  $r^2\text{SCAN}$ , similar to SCAN. Moreover, introducing the  $U$ -correction to SCAN and  $r^2\text{SCAN}$  increased the calculated lattice parameters, on-site magnetic moments, and the band gaps of the TMOs.

$r^2\text{SCAN}+U$  and  $\text{SCAN}+U$  successfully opened a band gap for narrow gap TMOs (except for  $\text{VO}_2$  and  $\text{Mn}_2\text{O}_3$  with  $r^2\text{SCAN}+U$ ). Upon testing the optimal  $U$  values with  $r^2\text{SCAN}+U$  on oxides with different oxidation states and/or coordination environments, we found that the  $U$  values derived in this work are in general transferable to other TM-containing oxides as well. Furthermore, we observed that  $r^2\text{SCAN}(+U)$  took less overall computational time (ionic +electronic steps) to converge when compared to SCAN, which indicated that  $r^2\text{SCAN}(+U)$  was computationally more efficient than  $\text{SCAN}(+U)$ . Since  $r^2\text{SCAN}+U$  offers a reasonably accurate prediction of material properties at a lower computational expense than  $\text{SCAN}+U$ , we observe that  $r^2\text{SCAN}+U$  can be used in high-throughput materials discovery, after adequate benchmarking tests are done in each new chemical space explored.

## ■ ASSOCIATED CONTENT

### Data Availability Statement

The data that support the findings of this study are openly available at our <https://github.com/sai-mat-group/r2SCAN-U-benchmarking> repository.

### Supporting Information

The Supporting Information is available free of charge at <https://pubs.acs.org/doi/10.1021/acs.jctc.3c00030>.

Details on the crystal structures used for calculations, oxidation energetics of Cr and Cu oxides, densities of states of all systems not showcased in the main text, and details on computational time calculations (PDF)

## ■ AUTHOR INFORMATION

### Corresponding Author

Gopalakrishnan Sai Gautam – Department of Materials Engineering, Indian Institute of Science, Bengaluru 560012, India; [orcid.org/0000-0002-1303-0976](https://orcid.org/0000-0002-1303-0976); Email: [saigautam@iisc.ac.in](mailto:saigautam@iisc.ac.in)

### Authors

S. Swathilakshmi – Department of Materials Engineering, Indian Institute of Science, Bengaluru 560012, India  
Reshma Devi – Department of Materials Engineering, Indian Institute of Science, Bengaluru 560012, India

Complete contact information is available at: <https://pubs.acs.org/10.1021/acs.jctc.3c00030>

### Author Contributions

G.S.G. envisioned and designed the work. S.S. and R.D. performed the calculations. All authors contributed to data analysis and writing the paper.

### Notes

The authors declare no competing financial interest.

## ■ ACKNOWLEDGMENTS

G.S.G. acknowledges the Indian Institute of Science (IISc) Seed Grant, SG/MHRD/20/0020 and SR/MHRD/20/0013, and the Science and Engineering Research Board (SERB) of the Department of Science and Technology, Government of India, under sanction numbers SRG/2021/000201 and IPA/2021/000007 for financial support. R.D. thanks the Ministry of Human Resource Development, Government of India, for financial assistance. S.S. acknowledges financial support from SERB under IPA/2021/000007. All the authors acknowledge the computational resources provided by the Supercomputer Education and Research Centre, IISc, for enabling some of the density functional theory calculations showcased in this work.

## ■ REFERENCES

- (1) Kohn, W.; Becke, A. D.; Parr, R. G. Density functional theory of electronic structure. *J. Phys. Chem.* **1996**, *100*, 12974–12980.
- (2) Jain, A.; Shin, Y.; Persson, K. A. Computational predictions of energy materials using density functional theory. *Nat. Rev. Mater.* **2016**, *1*, 15004.
- (3) Zhang, G.-X.; Reilly, A. M.; Tkatchenko, A.; Scheffler, M. Performance of various density-functional approximations for cohesive properties of 64 bulk solids. *New J. Phys.* **2018**, *20*, 063020.
- (4) Canepa, P.; Bo, S.-H.; Sai Gautam, G.; Key, B.; Richards, W. D.; Shi, T.; Tian, Y.; Wang, Y.; Li, J.; Ceder, G. High magnesium mobility in ternary spinel chalcogenides. *Nat. Commun.* **2017**, *8*, 1759.

- (5) Oganov, A. R.; Pickard, C. J.; Zhu, Q.; Needs, R. J. Structure prediction drives materials discovery. *Nat. Rev. Mater.* **2019**, *4*, 331–348.
- (6) Kirklın, S.; Meredig, B.; Wolverton, C. High-throughput computational screening of new Li-ion battery anode materials. *Adv. Energy Mater.* **2013**, *3*, 252–262.
- (7) Penev, E. S.; Marzari, N.; Yakobson, B. I. Theoretical prediction of two-dimensional materials, behavior, and properties. *ACS Nano* **2021**, *15*, 5959–5976.
- (8) Singh, M. R.; Goodpaster, J. D.; Weber, A. Z.; Head-Gordon, M.; Bell, A. T. Mechanistic insights into electrochemical reduction of CO<sub>2</sub> over Ag using density functional theory and transport models. *Proc. Natl. Acad. Sci. U.S.A.* **2017**, *114*, E8812–E8821.
- (9) Hasnip, P. J.; Refson, K.; Probert, M. I.; Yates, J. R.; Clark, S. J.; Pickard, C. J. Density functional theory in the solid state. *Philos. Trans. R. Soc. A* **2014**, *372*, 20130270.
- (10) Chan, M. K.; Wolverton, C.; Greeley, J. P. First principles simulations of the electrochemical lithiation and delithiation of faceted crystalline silicon. *J. Am. Chem. Soc.* **2012**, *134*, 14362–14374.
- (11) Zhou, J.-J.; Park, J.; Timrov, I.; Floris, A.; Cococcioni, M.; Marzari, N.; Bernardi, M. Ab Initio Electron-Phonon Interactions in Correlated Electron Systems. *Phys. Rev. Lett.* **2021**, *127*, 126404.
- (12) Bhattacharya, J.; Van der Ven, A. First-principles study of competing mechanisms of nondilute Li diffusion in spinel Li<sub>x</sub>Ti<sub>2</sub>S<sub>2</sub>. *Phys. Rev. B* **2011**, *83*, 144302.
- (13) Schindler, P.; Antoniuk, E. R.; Cheon, G.; Zhu, Y.; Reed, E. J. Discovery of materials with extreme work functions by high-throughput density functional theory and machine learning. 2020, arXiv:2011.10905. *arXiv preprint*. <https://arxiv.org/abs/2011.10905> (accessed 2023-06-15).
- (14) Gong, S.; Wang, S.; Xie, T.; Chae, W. H.; Liu, R.; Grossman, J. C. Calibrating DFT formation enthalpy calculations by multi-fidelity machine learning. 2021, arXiv:2110.13308. *arXiv preprint*. <https://arxiv.org/abs/2110.13308> (accessed 2023-06-15).
- (15) Ouyang, R.; Ahmetcik, E.; Carbogno, C.; Scheffler, M.; Ghiringhelli, L. M. Simultaneous learning of several materials properties from incomplete databases with multi-task SISSO. *J. Phys. Mater.* **2019**, *2*, 024002.
- (16) Park, C. W.; Wolverton, C. Developing an improved crystal graph convolutional neural network framework for accelerated materials discovery. *Phys. Rev. Mater.* **2020**, *4*, 063801.
- (17) Duan, C.; Liu, F.; Nandy, A.; Kulik, H. J. Putting density functional theory to the test in machine-learning-accelerated materials discovery. *J. Phys. Chem. Lett.* **2021**, *12*, 4628–4637.
- (18) Tran, F.; Stelzl, J.; Blaha, P. Rungs 1 to 4 of DFT Jacob's ladder: Extensive test on the lattice constant, bulk modulus, and cohesive energy of solids. *J. Chem. Phys.* **2016**, *144*, 204120.
- (19) Perdew, J. P.; Schmidt, K. Jacob's ladder of density functional approximations for the exchange-correlation energy. *AIP Conference Proceedings*; 2001; Vol. 577, pp 1–20.
- (20) Perdew, J. P.; Burke, K.; Ernzerhof, M. Generalized Gradient Approximation Made Simple. *Phys. Rev. Lett.* **1996**, *77*, 3865–3868.
- (21) Säßnick, H. D.; Cocchi, C. Electronic structure of cesium-based photocathode materials from density functional theory: Performance of PBE, SCAN, and HSE06 functionals. *Electron. struct.* **2021**, *3*, 027001.
- (22) Jadidi, Z.; Chen, T.; Xiao, P.; Urban, A.; Ceder, G. Effect of fluorination and Li-excess on the Li migration barrier in Mn-based cathode materials. *J. Mater. Chem. A* **2020**, *8*, 19965–19974.
- (23) Zhang, Q.; Khetan, A.; Er, S. Comparison of computational chemistry methods for the discovery of quinone-based electroactive compounds for energy storage. *Sci. Rep.* **2020**, *10*, 22149.
- (24) Sharkas, K.; Wagle, K.; Santra, B.; Akter, S.; Zope, R. R.; Baruah, T.; Jackson, K. A.; Perdew, J. P.; Peralta, J. E. Self-interaction error overbinds water clusters but cancels in structural energy differences. *Proc. Natl. Acad. Sci. U.S.A.* **2020**, *117*, 11283–11288.
- (25) Vargas, J.; Ufondu, P.; Baruah, T.; Yamamoto, Y.; Jackson, K. A.; Zope, R. R. Importance of self-interaction-error removal in density functional calculations on water cluster anions. *Phys. Chem. Chem. Phys.* **2020**, *22*, 3789–3799.
- (26) Isaacs, E. B.; Wolverton, C. *Phys. Rev. Mater.* **2018**, *2*, 063801.
- (27) Sarmiento-Perez, R.; Botti, S.; Marques, M. A. Optimized exchange and correlation semilocal functional for the calculation of energies of formation. *J. Chem. Theory Comput.* **2015**, *11*, 3844–3850.
- (28) Yang, Z.-h.; Peng, H.; Sun, J.; Perdew, J. P. More realistic band gaps from meta-generalized gradient approximations: Only in a generalized Kohn-Sham scheme. *Phys. Rev. B* **2016**, *93*, 205205.
- (29) Perdew, J. P.; Ruzsinszky, A.; Csonka, G. I.; Vydrov, O. A.; Scuseria, G. E.; Constantin, L. A.; Zhou, X.; Burke, K. Restoring the density-gradient expansion for exchange in solids and surfaces. *Phys. Rev. Lett.* **2008**, *100*, 136406.
- (30) Sun, J.; Ruzsinszky, A.; Perdew, J. Strongly Constrained and Appropriately Normed Semilocal Density Functional. *Phys. Rev. Lett.* **2015**, *115*, 036402.
- (31) Mejía-Rodríguez, D.; Trickey, S. B. Meta-GGA performance in solids at almost GGA cost. *Phys. Rev. B* **2020**, *102*, 121109.
- (32) Furness, J. W.; Kaplan, A. D.; Ning, J.; Perdew, J. P.; Sun, J. Accurate and Numerically Efficient r<sup>2</sup>SCAN Meta-Generalized Gradient Approximation. *J. Phys. Chem. Lett.* **2020**, *11*, 8208–8215.
- (33) Ehlert, S.; Huniar, U.; Ning, J.; Furness, J. W.; Sun, J.; Kaplan, A. D.; Perdew, J. P.; Brandenburg, J. G. r<sup>2</sup>SCAN-D4: Dispersion corrected meta-generalized gradient approximation for general chemical applications. *J. Chem. Phys.* **2021**, *154*, 061101.
- (34) Bartók, A. P.; Yates, J. R. Regularized SCAN functional. *J. Chem. Phys.* **2019**, *150*, 161101.
- (35) Furness, J. W.; Kaplan, A. D.; Ning, J.; Perdew, J. P.; Sun, J. Construction of meta-GGA functionals through restoration of exact constraint adherence to regularized SCAN functionals. *J. Chem. Phys.* **2022**, *156*, 034109.
- (36) Kingsbury, R.; Gupta, A. S.; Bartel, C. J.; Munro, J. M.; Dwaraknath, S.; Horton, M.; Persson, K. A. Performance comparison of r<sup>2</sup>SCAN and SCAN metaGGA density functionals for solid materials via an automated, high-throughput computational workflow. *Phys. Rev. Mater.* **2022**, *6*, 013801.
- (37) Kothakonda, M.; Kaplan, A. D.; Isaacs, E. B.; Bartel, C. J.; Furness, J. W.; Ning, J.; Wolverton, C.; Perdew, J. P.; Sun, J. Testing the r<sup>2</sup>SCAN Density Functional for the Thermodynamic Stability of Solids with and without a van der Waals Correction. *ACS Materials Au* **2023**, *3*, 102–111.
- (38) Sai Gautam, G.; Carter, E. A. Evaluating transition metal oxides within DFT-SCAN and SCAN+U frameworks for solar thermochemical applications. *Phys. Rev. Mater.* **2018**, *2*, 095401.
- (39) Long, O. Y.; Gautam, G. S.; Carter, E. A. Evaluating optimal U for 3d transition-metal oxides within the SCAN+U framework. *Phys. Rev. Mater.* **2020**, *4*, 045401.
- (40) Anisimov, V. I.; Zaanen, J.; Andersen, O. K. Band theory and Mott insulators: Hubbard U instead of Stoner I. *Phys. Rev. B* **1991**, *44*, 943–954.
- (41) Franchini, C.; Podloucky, R.; Paier, J.; Marsman, M.; Kresse, G. Ground-state properties of multivalent manganese oxides: Density functional and hybrid density functional calculations. *Phys. Rev. B* **2007**, *75*, 195128.
- (42) Timrov, I.; Marzari, N.; Cococcioni, M. Hubbard parameters from density-functional perturbation theory. *Phys. Rev. B* **2018**, *98*, 085127.
- (43) Cococcioni, M.; Gironcoli, S. D. Linear response approach to the calculation of the effective interaction parameters in the LDA+U method. *Phys. Rev. B* **2005**, *71*, 035105.
- (44) Zhou, F.; Cococcioni, M.; Marianetti, C. A.; Morgan, D.; Ceder, G. First-principles prediction of redox potentials in transition-metal compounds with LDA+U. *Phys. Rev. B* **2004**, *70*, 235121.
- (45) Moore, G. C.; Horton, M. K.; Ganose, A. M.; Siron, M.; Persson, K. A. High-throughput determination of Hubbard U and Hund J. values for transition metal oxides via linear response formalism. 2022, arXiv:2201.04213. *arXiv preprint*. <https://arxiv.org/abs/2201.04213> (accessed 2023-06-15).

- (46) Mosey, N. J.; Carter, E. A. Ab initio evaluation of Coulomb and exchange parameters for DFT+U calculations. *Phys. Rev. B* **2007**, *76*, 155123.
- (47) Mosey, N. J.; Liao, P.; Carter, E. A. Rotationally invariant ab initio evaluation of Coulomb and exchange parameters for DFT+U calculations. *J. Chem. Phys.* **2008**, *129*, 014103.
- (48) Yu, M.; Yang, S.; Wu, C.; Marom, N. Machine learning the Hubbard  $U$  parameter in DFT+U using Bayesian optimization. *npj Comput. Mater.* **2020**, *6*, 180.
- (49) Artrith, N.; Torres, J. A. G.; Urban, A.; Hybertsen, M. S. Data-driven approach to parameterize SCAN+U for an accurate description of 3d transition metal oxide thermochemistry. *Phys. Rev. Mater.* **2022**, *6*, 035003.
- (50) Hafner, J.; Kresse, G. *Vienna AB-Initio Simulation Program VASP: An Efficient and Versatile Tool for Studying the Structural, Dynamic, and Electronic Properties of Materials* **1997**, 69–82.
- (51) Kresse, G.; Hafner, J. Ab initio molecular dynamics for liquid metals. *Phys. Rev. B* **1993**, *47*, 558–561.
- (52) Kresse, G.; Furthmüller, J. Efficient iterative schemes for ab initio total-energy calculations using a plane-wave basis set. *Phys. Rev. B* **1996**, *54*, 11169–11186.
- (53) Kresse, G.; Joubert, D. From ultrasoft pseudopotentials to the projector augmented-wave method. *Phys. Rev. B* **1999**, *59*, 1758–1775.
- (54) Monkhorst, H. J.; Pack, J. D. Special points for Brillouin-zone integrations. *Phys. Rev. B* **1976**, *13*, 5188–5192.
- (55) Dudarev, S. L.; Botton, G. A.; Savrasov, S. Y.; Humphreys, C. J.; Sutton, A. P. Electron-energy-loss spectra and the structural stability of nickel oxide: An LSDA+U study. *Phys. Rev. B* **1998**, *57*, 1505–1509.
- (56) Kitchaev, D. A.; Peng, H.; Liu, Y.; Sun, J.; Perdew, J. P.; Ceder, G. Energetics of MnO<sub>2</sub> polymorphs in density functional theory. *Phys. Rev. B* **2016**, *93*, 045132.
- (57) Perdew, J. P.; Yang, W.; Burke, K.; Yang, Z.; Gross, E. K.; Scheffler, M.; Scuseria, G. E.; Henderson, T. M.; Zhang, I. Y.; Ruzsinszky, A.; Peng, H.; Sun, J.; Trushin, E.; Görling, A. Understanding band gaps of solids in generalized Kohn-Sham theory. *Proc. Natl. Acad. Sci. U.S.A.* **2017**, *114*, 2801–2806.
- (58) Kubaschewski, O.; Alcock, C. B. *Materials Thermochemistry*; Pergamon Press Ltd.: Headington Hill Hall, Oxford, 1993.
- (59) Barin, I. *Thermochemical Data of Pure Substances*; John Wiley & Sons Ltd.: New York, USA, 1995; pp I–L.
- (60) Wagman, D.; Evans, W.; Parker, V.; Schumm, R.; Halow, I.; Bailey, S.; Churney, K.; Nuttall, R. *The NBS Tables of Chemical Thermodynamic Properties: Selected Values for Inorganic and C1 and C2 Organic Substances in SI Units*; American Chemical Society and the American Institute of Physics for the National Bureau of Standards: Washington, DC, 1982, Vol. 11.
- (61) Hellenbrandt, M. The Inorganic Crystal Structure Database (ICSD)-Present and Future. *Crystallogr. Rev.* **2004**, *10*, 17–22.
- (62) Coey, J.; Venkatesan, M. Half-metallic ferromagnetism: Example of CrO<sub>2</sub>. *J. Appl. Phys.* **2002**, *91*, 8345–8350.
- (63) Rogers, K. D. An X-ray diffraction study of semiconductor and metallic vanadium dioxide. *Powder Diffr.* **1993**, *8*, 240–244.
- (64) Sasaki, S.; Takeuchi, Y.; Fujino, K. X-Ray Determination of Electron Density Distributions in Oxides, MgO, MnO, CoO, and NiO, and Atomic Scattering Factors of their Constituent Atoms. *Proc. Jpn. Acad., Ser. B* **1979**, *55*, 43–48.
- (65) Kuriyama, M.; Hosoya, S. X-ray measurement of scattering factors of manganese and oxygen atoms in manganous oxide. *J. Phys. Soc. Jpn.* **1962**, *17*, 1022–1029.
- (66) Jauch, W.; Reehuis, M.; Bleif, H. J.; Kubanek, F.; Pattison, P. Crystallographic symmetry and magnetic structure of CoO. *Phys. Rev. B* **2001**, *64*, 052102.
- (67) Shen, Z. X.; List, R. S.; Dessau, D. S.; Wells, B. O.; Jepsen, O.; Arko, A. J.; Bartlett, R.; Shih, C. K.; Parmigiani, F.; Huang, J. C.; Lindberg, P. A. Electronic structure of NiO: Correlation and band effects. *Phys. Rev. B* **1991**, *44*, 3604–3626.
- (68) Fjellvåg, H.; Grønvd, F.; Stølen, S.; Hauback, S. On the crystallographic and magnetic structures of nearly stoichiometric iron monoxide. *J. Solid State Chem.* **1996**, *124*, 52–57.
- (69) Hartmann, H.; Mässung, W. Elektrolyse in Phosphatschmelzen. IV. Über die Elektrolyse von Vanadin-, Niob- und Tantaloxyd in Phosphatschmelzen. *Z. Anorg. Allg. Chem.* **1951**, *266*, 98–104.
- (70) Ghijsen, J.; Tjeng, L. H.; Elp, J. V.; Eskes, H.; Westerink, J.; Sawatzky, G. A.; Czyzyk, M. T. Electronic structure of Cu<sub>2</sub>O and CuO. *Phys. Rev. B* **1988**, *38*, 11322–11330.
- (71) Mittal, R.; Chaplot, S. L.; Mishra, S. K.; Bose, P. P. Inelastic neutron scattering and lattice dynamical calculation of negative thermal expansion compounds Cu<sub>2</sub>O and Ag<sub>2</sub>O. *Phys. Rev. B* **2007**, *75*, 174303.
- (72) Regulski, M.; Przeniosło, R.; Sosnowska, I.; Hoffmann, J.-U. Incommensurate magnetic structure of  $\beta$ -MnO<sub>2</sub>. *Phys. Rev. B* **2003**, *68*, 172401.
- (73) Loehman, R.; Rao, C. R.; Honig, J. M. Crystallography and defect chemistry of solid solutions of vanadium and titanium oxides. *J. Phys. Chem.* **1969**, *73*, 1781–1784.
- (74) Rozier, P.; Ratuszna, A.; Galy, J. Comparative Structural and Electrical Studies of V<sub>2</sub>O<sub>3</sub> and V<sub>2-x</sub>Ni<sub>x</sub>O<sub>3</sub> (0 < x < 0.75) Solid Solution. *Z. Anorg. Allg. Chem.* **2002**, *628*, 1236–1242.
- (75) Ashkenazi, J.; Chuchem, T. Band structure of V<sub>2</sub>O<sub>3</sub>, and Ti<sub>2</sub>O<sub>3</sub>. *Philos. Mag.* **1975**, *32*, 763–785.
- (76) Maslen, E. N.; Streltsov, V. A.; Streltsova, N. R.; Ishizawa, N. Synchrotron X-ray study of the electron density in  $\alpha$ -Fe<sub>2</sub>O<sub>3</sub>. *Acta Crystallogr., Sect. B* **1994**, *50*, 435–441.
- (77) Brockhouse, B. N. Antiferromagnetic structure in Cr<sub>2</sub>O<sub>3</sub>. *J. Chem. Phys.* **1953**, *21*, 961–962.
- (78) Abrahams, S. C. Magnetic and crystal structure of titanium sesquioxide. *Phys. Rev.* **1963**, *130*, 2230–2237.
- (79) Verwey, E. J. W. Electronic conduction of magnetite (Fe<sub>3</sub>O<sub>4</sub>) and its transition point at low temperatures. *Nature* **1939**, *144*, 327–328.
- (80) Park, S. K.; Ishikawa, T.; Tokura, Y. Charge-gap formation upon the Verwey transition in Fe<sub>3</sub>O<sub>4</sub>. *Phys. Rev. B* **1998**, *58*, 3717.
- (81) Smith, W. L.; Hobson, A. D. The structure of cobalt oxide, Co<sub>3</sub>O<sub>4</sub>. *Acta Crystallogr., Sect. B* **1973**, *29*, 362–363.
- (82) Knop, O.; Reid, K.; Sutarno; Nakagawa, Y. Chalkogenides of the transition elements. VI. X-Ray, neutron, and magnetic investigation of the spinels Co<sub>3</sub>O<sub>4</sub>, NiCo<sub>2</sub>O<sub>4</sub>, Co<sub>3</sub>S<sub>4</sub>, and NiCo<sub>2</sub>S<sub>4</sub>. *Can. J. Chem.* **1968**, *46*, 3463.
- (83) Roth, W. L. The magnetic structure of Co<sub>3</sub>O<sub>4</sub>. *J. Phys. Chem. Solids* **1964**, *25*, 1–10.
- (84) Patton, D. C.; Porezag, D. V.; Pederson, M. R. Simplified generalized-gradient approximation and anharmonicity: Benchmark calculations on molecules. *Phys. Rev. B* **1997**, *55*, 7454–7459.
- (85) Wang, M.; Navrotsky, A. Enthalpy of formation of LiNiO<sub>2</sub>, LiCoO<sub>2</sub> and their solid solution, LiNi<sub>1-x</sub>Co<sub>x</sub>O<sub>2</sub>. *Solid State Ion.* **2004**, *166*, 167–173.
- (86) Pople, J. A.; Head-Gordon, M.; Fox, D. J.; Raghavachari, K.; Curtiss, L. A. Gaussian-1 theory: A general procedure for prediction of molecular energies. *J. Chem. Phys.* **1989**, *90*, 5622–5629.
- (87) Giannozzi, P.; Car, R.; Scoles, G. Oxygen adsorption on graphite and nanotubes. *J. Chem. Phys.* **2003**, *118*, 1003–1006.
- (88) Hammer, B.; Hansen, L. B.; Nørskov, J. K. Improved adsorption energetics within density-functional theory using revised Perdew-Burke-Ernzerhof functionals. *Phys. Rev. B* **1999**, *59*, 7413–7421.
- (89) Wang, L.; Maxisch, T.; Ceder, G. Oxidation energies of transition metal oxides within the GGA+U framework. *Phys. Rev. B* **2006**, *73*, 195107.
- (90) Rahaman, H.; Laha, R. M.; Maiti, D. K.; Ghosh, S. K. Fabrication of Mn<sub>2</sub>O<sub>3</sub> nanorods: an efficient catalyst for selective transformation of alcohols to aldehydes. *RSC Adv.* **2015**, *5*, 33923–33929.
- (91) Javed, Q.-u.-a.; Feng-Ping, W.; Rafique, M. Y.; Toufiq, A. M.; Iqbal, M. Z. Canted antiferromagnetic and optical properties of

nanostructures of  $\text{Mn}_2\text{O}_3$  prepared by hydrothermal synthesis. *Chin. Phys. B* **2012**, *21*, 117311.

(92) Bland, J. A. The crystal structure of barium orthotitanate,  $\text{Ba}_2\text{TiO}_4$ . *Acta Crystallogr.* **1961**, *14*, 875–881.

(93) Shanker, V.; Ahmad, T.; Ganguli, A. K. Investigation of  $\text{Ba}_{2-x}\text{Sr}_x\text{TiO}_4$ : Structural aspects and dielectric properties. *Bull. Mater. Sci.* **2004**, *27*, 421–427.

(94) Liu, T.; Zhang, X.; Guan, J.; Catlow, C. R. A.; Walsh, A.; Sokol, A. A.; Buckeridge, J. Insight into the Fergusonite-Scheelite Phase Transition of  $\text{ABO}_4$ -Type Oxides by Density Functional Theory: A Case Study of the Subtleties of the Ground State of  $\text{BiVO}_4$ . *Chem. Mater.* **2022**, *34*, 5334–5343.

(95) Bhattacharya, A. K.; Mallick, K. K.; Hartridge, A. Phase transition in  $\text{BiVO}_4$ . *Mater. Lett.* **1997**, *30*, 7–13.

(96) Cooper, J. K.; Gul, S.; Toma, F. M.; Chen, L.; Glans, P.-A.; Guo, J.; Ager, J. W.; Yano, J.; Sharp, I. D. Electronic Structure of Monoclinic  $\text{BiVO}_4$ . *Chem. Mater.* **2014**, *26*, 5365–5373.

(97) Lawler, K. V.; Childs, B. C.; Mast, D. S.; Czerwinski, K. R.; Sattelberger, A. P.; Poineau, F.; Forster, P. M. Molecular and Electronic Structures of  $\text{M}_2\text{tO}_7$  ( $\text{M} = \text{Mn, Tc, Re}$ ). *Inorg. Chem.* **2017**, *56*, 2448–2458.

(98) Simon, A.; Dronskowski, R.; Krebs, B.; Hettich, B. The Crystal Structure of  $\text{Mn}_2\text{tO}_7$ . *Angew. Chem., Int. Ed.* **1987**, *26*, 139–140.

(99) Olazcuaga, R.; Reau, J.-M.; Leflem, G.; Hagenmuller, P. Préparation, Propriétés Cristallographiques et Magnétiques des Phases  $\text{K}_3\text{XO}_4$  ( $\text{X} = \text{V, Cr, Mn}$ ). *Z. Anorg. Allg. Chem.* **1975**, *412*, 271–280.

(100) Palenik, G. J. Crystal structure of potassium manganate. *Inorg. Chem.* **1967**, *6*, 507–511.

(101) Takeda, T.; Yamaguchi, Y.; Watanabe, H. Magnetic Structure of  $\text{SrFeO}_3$ . *J. Phys. Soc. Jpn.* **1972**, *33*, 967–969.

(102) Shein, I. R.; Shein, K. I.; Kozhevnikov, V. L.; Ivanovskii, A. L. Band structure and the magnetic and elastic properties of  $\text{SrFeO}_3$  and  $\text{LaFeO}_3$  perovskites. *Phys. Solid State* **2005**, *47*, 2082–2088.

(103) Amatucci, G. G.; Tarascon, J. M.; Klein, L. C.  $\text{CoO}_2$ , The End Member of the  $\text{Li}_x\text{CoO}_2$  Solid Solution. *J. Electrochem. Soc.* **1996**, *143*, 1114–1123.

(104) Delmas, C.; Ménétrier, M.; Croguennec, L.; Levasseur, S.; Pérès, J. P.; Poullierie, C.; Prado, G.; Fournés, L.; Weill, F. Lithium batteries: a new tool in solid state chemistry. *Int. J. Inorg. Mater.* **1999**, *1*, 11–19.

(105) Aydinol, M. K.; Kohan, A. F.; Ceder, G.; Cho, K.; Joannopoulos, J. Ab initio study of lithium intercalation in metal oxides and metal dichalcogenides. *Phys. Rev. B* **1997**, *56*, 1354–1365.

(106) Long, O. Y.; Sai Gautam, G.; Carter, E. A. Assessing cathode property prediction via exchange-correlation functionals with and without long-range dispersion corrections. *Phys. Chem. Chem. Phys.* **2021**, *23*, 24726–24737.

(107) Delmas, C.; Ménétrier, M.; Croguennec, L.; Levasseur, S.; Pérès, J.; Poullierie, C.; Prado, G.; Fournés, L.; Weill, F. Lithium batteries: a new tool in solid state chemistry. *Int. J. Inorg. Mater.* **1999**, *1*, 11–19.

(108) Ohzuku, T.; Ueda, A. Why transition metal (di) oxides are the most attractive materials for batteries. *Solid State Ion.* **1994**, *69*, 201–211.

(109) Aydinol, M.; Kohan, A.; Ceder, G. Ab initio calculation of the intercalation voltage of lithium-transition-metal oxide electrodes for rechargeable batteries. *J. Power Sources* **1997**, *68*, 664–668.

(110) Arroyo y de Dompablo, M. E.; Van der Ven, A.; Ceder, G. First-principles calculations of lithium ordering and phase stability on  $\text{Li}_x\text{NiO}_2$ . *Phys. Rev. B* **2002**, *66*, 064112.